NASA TECHNICAL NOTE

NASA TN D-7728

NASA TN D-7728

NUMERICAL AND EXPERIMENTAL STUDIES OF THE NATURAL CONVECTION WITHIN A HORIZONTAL CYLINDER

by Roger B. Stewart, Alexander P. Sabol, and Lillian R. Boney

Langley Research Center
Hampton, Va. 23665

NATIONAL AERONAUTICS AND SPACE ADMINISTRATION • WASHINGTON, D. C. • DECEMBER 1974

1. Report No.	2. Government Accession No.	3. Recipient's Catalog No.
NASA TN D-7728		

4. Title and Subtitle	5. Report Date
NUMERICAL AND EXPERIMENTAL STUDIES OF THE NATURAL CONVECTION WITHIN A HORIZONTAL CYLINDER	December 1974
	6. Performing Organization Code
7. Author(s)	8. Performing Organization Report No.
Roger B. Stewart, Alexander P. Sabol, and Lillian R. Boney	L-9652
	10. Work Unit No.
9. Performing Organization Name and Address	501-04-03-06
NASA Langley Research Center Hampton, Va. 23665	11. Contract or Grant No.
	13. Type of Report and Period Covered
12. Sponsoring Agency Name and Address	Technical Note
National Aeronautics and Space Administration Washington, D.C. 20546	14. Sponsoring Agency Code

15. Supplementary Notes

16. Abstract

Numerical solutions are obtained for the quasi-compressible Navier-Stokes equations governing the time-dependent natural convection within a horizontal cylinder. The early flow development and wall heat transfer are obtained after a uniformly cold wall is imposed as a boundary condition on the cylinder. Results are also obtained for a time-varying cold wall as a boundary condition with windward explicit differencing used for the numerical solutions. The viscous truncation error associated with this scheme is controlled so that first-order accuracy is maintained in time and space. The results encompass a range of Grashof number from 8.34×10^4 to 7×10^7, which is within the laminar flow regime for gravitationally driven fluid flows. Experiments within a small-scale instrumented horizontal cylinder revealed the time development of the temperature distribution across the boundary layer as well as the decay of wall heat transfer with time. Agreement between temperature distributions obtained experimentally and numerically was generally good. The time decay of the dimensionless ratio of the Nusselt number to the one-fourth power of the Grashof number is found both numerically and experimentally, and good agreement is obtained between these two results over most of the cylinder wall. The numerical results indicate that the fluid exhibits a strong tendency to resist first-order motion within the inner core region. The early establishment of a shallow, positive, upward temperature gradient within the core enhances its stability. No first-order vortical motion is induced by the boundary layer and this is attributed in part to the fluid deceleration near the bottom of the cylinder along with expulsion of fluid from the boundary layer in the lower portions of the cylinder.

17. Key Words (Suggested by Author(s))	18. Distribution Statement
Confined natural connection Heat transfer Cylindrical geometry Experimental and numerical results	Unclassified – Unlimited STAR Category 12

19. Security Classif. (of this report)	20. Security Classif. (of this page)	21. No. of Pages	22. Price*
Unclassified	Unclassified	64	$4.25

*For sale by the National Technical Information Service, Springfield, Virginia 22151

CONTENTS

NUMERICAL AND EXPERIMENTAL STUDIES OF THE NATURAL CONVECTION WITHIN A HORIZONTAL CYLINDER

By Roger B. Stewart, Alexander P. Sabol, and Lillian R. Boney
Langley Research Center

SUMMARY

Numerical solutions are obtained for the quasi-compressible Navier-Stokes equations governing the time-dependent natural convection within a horizontal cylinder. The early flow development and wall heat transfer are obtained after a uniformly cold wall is imposed as a boundary condition on the cylinder. Results are also obtained for a time-varying cold wall as a boundary condition with windward explicit differencing used for the numerical solutions. The viscous truncation error associated with this scheme is controlled so that first-order accuracy is maintained in time and space. The results encompass a range of Grashof number from 8.34×10^4 to 7×10^7, which is within the laminar flow regime for gravitationally driven fluid flows. Experiments within a small-scale instrumented horizontal cylinder revealed the time development of the temperature distribution across the boundary layer as well as the decay of wall heat transfer with time. Agreement between temperature distributions obtained experimentally and numerically was generally good. The time decay of the dimensionless ratio of the Nusselt number to the one-fourth power of the Grashof number is found both numerically and experimentally, and good agreement is obtained between these two results over most of the cylinder wall. The numerical results indicate that the fluid exhibits a strong tendency to resist first-order motion within the inner core region. The early establishment of a shallow, positive, upward temperature gradient within the core enhances its stability. No first-order vortical motion is induced by the boundary layer and this is attributed in part to the fluid deceleration near the bottom of the cylinder along with expulsion of fluid from the boundary layer in the lower portions of the cylinder.

INTRODUCTION

Natural convection of fluids within closed systems has been extensively studied during the past 20 years. Reference 1 provides a detailed account of the work done prior to 1964. More recently, numerical solutions and experiments have provided insight into the fluid behavior for a variety of wall boundary conditions in enclosed systems under steady-state conditions (refs. 2 to 6).

The work concerning flow within cylindrical geometries reported in references 2, 3, 5, and 6 has attempted to relate the dimensionless heat transfer, or Nusselt number, to the Grashof number, which describes the ratio of thermally driven gravitational effects to fluid viscous effects. A number of nonuniform wall boundary conditions have been investigated for the purpose of gaining insight into the coupling between the inner core flow and the primary gravitationally driven flow that occurs within the wall boundary layer. These studies have dealt exclusively with steady-state fluid flows.

A problem closely related to the one in the present study is reported in reference 4, where numerical solutions were obtained for a horizontal cylinder with one-half of the cylinder wall heated and one-half cooled. Both the unsteady and steady-state flow were studied numerically, but comparisons with experiments were obtained only for the steady-state conditions. Very little work has been reported that compares the numerical and experimental development of unsteady natural convection in enclosed systems.

The purpose of the present study was to investigate the fluid motion and wall heat transfer for a uniformly cold wall that was imposed as an initial condition at time zero. The resulting two-dimensional, unsteady laminar fluid flow is an idealization of the problem first reported in reference 7, which considered the feasibility of developing a facility using stored arc-heated air to duplicate Mach 8 to 10 flight conditions. The heat loss to the walls of a large storage tank resulting from natural convection could conceivably place a size and input-power restriction on the development of such a facility. The need for a detailed understanding of the fluid behavior in a storage chamber motivated the present study. The development of the numerical solution technique is described in reference 8 and a stability analysis of the coupled finite-difference equations is presented. The present work provides numerical results describing the unsteady velocity- and thermal-field behavior within a horizontal cylinder and includes a quantitative assessment of the early fluid stratification that leads to a positive vertical temperature distribution in the core flow. Experimental measurements of the thermal behavior of the fluid were made within a small-scale horizontal cylinder.

SYMBOLS

A	area
c	specific heat of cylinder wall material
c_p	specific heat at constant pressure

c_w dimensionless constant (called dimensionless heat-transfer group in ref. 4).

$$c_w = \frac{N_{Nu}}{N_{Gr}^{1/4}}$$

d diameter of cylinder

g gravitational acceleration

h heat-transfer coefficient

k thermal conductivity

ℓ length

N_{Gr} Grashof number, $\frac{g r_w^3}{\nu_i^2} \frac{T_i - T_w}{T_i}$

N_{Nu} Nusselt number, $\frac{hd}{k}$

N_{Pr} Prandtl number, $\frac{c_p \mu}{k}$

p pressure

$\tilde{p}$ dimensionless pressure, $\frac{p}{g \beta \alpha \rho_i r_w}$

q dynamic pressure

$\tilde{q}$ dimensionless dynamic pressure, $\frac{q}{g \beta \alpha \rho_i r_w}$

r radial distance from center of cylinder

$\tilde{r}$ dimensionless radial distance from center of cylinder

$\Delta\tilde{r}$ dimensionless distance between two successive radial grid points

t time

$\tilde{t}$ dimensionless time, $t\sqrt{\frac{g \beta \alpha}{r_w}}$

$\Delta\tilde{t}$ dimensionless time increment

T temperature

T_{xo} temperature of outer wall surface given by equation (13)

u azimuthal velocity component

$\tilde{u}$ dimensionless azimuthal velocity component, $\dfrac{u}{\sqrt{g\beta\alpha r_w}}$

v radial velocity component

$\tilde{v}$ dimensionless radial velocity component, $\dfrac{v}{\sqrt{g\beta\alpha r_w}}$

x distance from inner surface of cylinder wall toward outer wall surface

α temperature difference, $T_i - T_w$

$\beta = \dfrac{1}{T_i}$

θ azimuthal coordinate

$\Delta\theta$ distance between two successive azimuthal grid points

μ dynamic viscosity

ν kinematic viscosity

ρ fluid density

$\tilde{\rho}$ dimensionless fluid density, ρ/ρ_i

ϕ dimensionless temperature function, $\dfrac{T_i - T}{T_i - T_w}$

Φ dimensionless temperature function, $\dfrac{T_w - T_{xo}}{T_i - T_{xo}}$

Subscripts:

i initial value at time zero

min	minimum
max	maximum
w	value at cylinder wall

PHYSICAL DESCRIPTION OF THE PROBLEM

The geometry and nomenclature of the horizontal cylinder to be studied are shown in figure 1. The cylinder is of infinite length to allow a region of two-dimensional flow to exist.[1] When a hot gas is stored in a horizontal cylinder, appreciable azimuthal gas flow occurs because of the imbalance between the gravitational body forces and the existing hydrostatic pressure gradient in the fluid. The gas is initially at rest with a balance between the body forces and the hydrostatic pressure gradient and is initially at a uniform temperature T_i. At time zero a uniformly cold wall is imposed on the cylinder and the resulting conduction of heat out of the gas near the wall causes the convective motion to begin. As the flow develops, a thin boundary layer is formed at the wall and thickens with time. The initially motionless inner fluid (the core) is driven by the boundary-layer flow and gives up energy to the heat-conducting boundary-layer fluid. At large values of time, the boundary layer will affect the innermost regions of the core flow, and eventually the gas can be expected to give up all its excess energy to the cold wall. Although these late values of time are not studied here, it can be anticipated that the fluid will be once again at rest with a uniform temperature equal to the wall temperature.

Several distinct features are intuitively apparent. Because of the uniform wall temperature, a plane of symmetry, with the dividing line running vertically upward through the center of the cylinder, is immediately established. For the azimuthal velocity component, a stagnation line coincides with the midplane of symmetry. In each half-cylinder there are two stagnation points which will be at the intersection of the midplane of symmetry and the wall. For a no-slip wall boundary condition these points will not appear as singularities because they are immersed in the boundary layer at its very limit, the wall.

The principal motion in the boundary layer will be azimuthal and the induced motion will be radial. Because of the small coefficient of viscosity for air, very low velocities in the core may be expected. Both inward and outward radial velocities will occur across

[1] A two-dimensional flow within a horizontal cylinder has been observed by Brooks and Ostrach (ref. 6).

the boundary layer. In addition, it might be anticipated that some stratification of the flow will occur in the lower portions of the cylinder.

THE GOVERNING EQUATIONS

The model chosen for this study is that of a viscous, heat-conducting, quasi-compressible fluid that conforms to the Boussinesq approximation. For small differences between the gas temperature and the wall temperature, the density may be taken as a function of temperature only and considered as a variable only where it modifies the body-force terms in the equations describing conservation of momentum. This approximation has been investigated extensively in references 3, 4, and 9 to 11.

The quasi-compressible Navier-Stokes equations applicable to the case of large Grashof numbers and small differences between gas and wall temperatures, in cylindrical coordinates and in nondimensional form, are

Azimuthal momentum,

$$\frac{\partial \tilde{u}}{\partial \tilde{t}} + \frac{v}{\tilde{r}}\frac{\partial \tilde{u}}{\partial \tilde{r}} + \frac{\tilde{u}}{\tilde{r}}\frac{\partial \tilde{u}}{\partial \theta} = -\phi \sin\theta - \frac{1 - \phi\beta\alpha}{\tilde{r}}\frac{\partial \tilde{q}}{\partial \theta} + \frac{1}{\sqrt{N_{Gr}}}\left(\frac{\partial^2 \tilde{u}}{\partial \tilde{r}^2} + \frac{1}{\tilde{r}}\frac{\partial \tilde{u}}{\partial \tilde{r}} - \frac{\tilde{u}}{\tilde{r}^2} + \frac{1}{\tilde{r}^2}\frac{\partial^2 \tilde{u}}{\partial \theta^2}\right) \tag{1}$$

Radial momentum,

$$\frac{\partial \tilde{q}}{\partial \tilde{r}} = \frac{\tilde{u}^2}{\tilde{r}} - \phi \cos\theta \tag{2}$$

Mass continuity,

$$\frac{\partial(\tilde{r}\tilde{v})}{\partial \tilde{r}} + \frac{\partial \tilde{u}}{\partial \theta} = 0 \tag{3}$$

Energy,

$$\frac{\partial \phi}{\partial \tilde{t}} + \frac{\tilde{v}}{\tilde{r}}\frac{\partial \phi}{\partial \tilde{r}} + \frac{\tilde{u}}{\tilde{r}}\frac{\partial \phi}{\partial \theta} = \frac{1}{N_{Pr}\sqrt{N_{Gr}}}\frac{\partial^2 \phi}{\partial \tilde{r}^2} \tag{4}$$

State,

$$\tilde{\rho} = \frac{1}{1 - \beta\alpha\phi} \tag{5}$$

Initial conditions (at $\tilde{t} = 0$):

$$\left.\begin{aligned} &\tilde{u} = \tilde{v} = 0 \\ &\phi = 0 \\ &\tilde{q} = 0 \end{aligned}\right\} \tag{6}$$

Boundary conditions

At $\tilde{r} = 1.0$:

$$\left.\begin{aligned} &\tilde{u} = \tilde{v} = 0 \\ &\phi = 1.0 \\ &\tilde{q} = \tilde{q}_w \end{aligned}\right\} \tag{7}$$

On $\theta = 0$ and π:

$$\frac{\partial \tilde{u}}{\partial \theta} = \frac{\partial \tilde{v}}{\partial \theta} = \frac{\partial \phi}{\partial \theta} = 0 \tag{8}$$

The derivation of the system of equations (1) to (5) is given in reference 8 along with a justification for neglecting terms in both the momentum and energy equations that are known to be negligible for gravitationally driven fluid flows.

Equations (1) to (5) along with the initial and boundary conditions given by equations (6) to (8) were solved by means of an explicit windward-differencing scheme that has been described in references 4, 8, 12, and 13. The formulation of the difference equations and a stability analysis are presented in reference 8. From the stability analysis given in reference 8, a minimum allowable time step was determined to be

$$\Delta\tilde{t} \leqq \frac{1}{\dfrac{2|\tilde{u}|}{\tilde{r}\,\Delta\theta} + \dfrac{2|\tilde{v}|}{\Delta\tilde{r}} + \dfrac{4}{\sqrt{N_{Gr}}(\tilde{r}\,\Delta\theta)^2} + \dfrac{4}{\sqrt{N_{Gr}}\,\Delta\tilde{r}^2}} \tag{9}$$

The time step chosen for the calculations was 0.8 of the value for $\Delta\tilde{t}$ given by equation (9).

The dimensionless heat transfer at the wall was obtained from

$$h = \frac{\dot{q}}{A\left(T_i - T_w\right)} \tag{10}$$

(where $\dot{q}$ is the heat-transfer rate) or

$$h = -\frac{k}{T_i - T_w}\left(\frac{\partial T}{\partial r}\right)_{\substack{r = r_w \\ \theta = \text{Constant}}} \tag{11}$$

Thus,

$$N_{Nu} = \frac{2}{\left(T_i - T_w\right)}\left(\frac{\partial T}{\partial \tilde{r}}\right)_{\substack{\tilde{r} = 1 \\ \theta = \text{Constant}}} \tag{12}$$

where the derivative obtained from the difference-equation solutions was evaluated from the wall into the flow. Figure 2 shows a typical finite-difference grid network for one-half of the cylinder. Because of the symmetry about the midplane, calculations need only be made over half the cylinder as shown.

NUMERICAL RESULTS

The difference equations corresponding to the system (1) to (9) were solved for values of $\tilde{u}$, $\tilde{v}$, ϕ, and $\tilde{q}$ over the entire grid after a uniformly cold wall was imposed as a condition at time zero. Equation (12) was solved for each time increment following time zero to provide dimensionless values of wall heat transfer. Three different grid sizes were used to study the difference approximation to the differential equations. These grid sizes were 31 by 51, 31 by 101, and 31 by 151, with the azimuthal grid remaining unchanged at a value of 31. The Control Data series 6600 computer system at the Langley Research Center was used. Typical computational times were 1.02×10^7 grid point solutions per hour obtained for the 31 by 51 grid network. The real-time flow developed at a rate of about 1.25 seconds per hour of machine time for the early flow development.

Input Values

Table I lists the values of the input parameters that were used for the solutions to be presented. The values chosen for cases I and II resulted from the experimental conditions that were to be employed for comparison between the numerical results and measured

values. For cases I and II the variable Grashof numbers and wall temperatures shown are described later in this section.

Constant Wall Temperature

For the cases with constant wall temperature listed in table I, a step-function cold-wall condition was imposed over the entire wall at time zero. Figure 3(a) shows the azimuthal velocity distribution for case I and three different values of time at the azimuthal location $\theta = 90^{\circ}$. The early time $(\tilde{t} = 3.05)$ shows the distribution prior to the development of peak azimuthal velocities. By this it is meant that peak velocities at any location have not been achieved. The intermediate time $(\tilde{t} = 4.57)$ shows the azimuthal velocity distribution at its peak value, and the late time $(\tilde{t} = 14.5)$ shows the distributions after a decay in the velocity has taken place. Significant inward displacements of the maximum velocity are not apparent; however, the boundary layer thickens with time over about 20 grid point spacings for the 31 by 51 grid used. The viscous effects are transported farther into the core of the fluid as time progresses.

The distributions shown in figure 3 are typical of all the results obtained for a constant wall temperature. Figure 3(b) shows the velocity distribution near the bottom of the cylinder at an azimuthal angle of 23.7°. The momentum gathered by the fluid falling downward has both thickened the boundary layer and increased the peak azimuthal velocity. At values of θ less than 23°, the fluid rapidly decelerates and comes nearly to rest in the lower part of the cylinder. Figure 3(c) shows the velocity distribution near the top of the cylinder. The boundary layer is well defined, but the azimuthal velocities are substantially lower than in the bottom portion of the cylinder near the wall.

Figure 4(a) shows the radial velocity distribution for case I of table I. Here it is seen that the peak velocities are an order of magnitude less than corresponding azimuthal velocities. The radial velocities peak at the later time $(\tilde{t} = 14.5)$ in contrast to the azimuthal velocities, which peak near $\tilde{t} = 4.57$. The negative radial velocity in figure 4(b) at $\theta = 23.7^{\circ}$ indicates an expulsion of fluid from the boundary layer. As the lower portion of the cylinder "fills" with fluid that has moved downward in the boundary layer, negative or inward radial flow takes place to accommodate the added fluid. Thus fluid is slowly forced into the boundary layer near the top of the cylinder because of displacement effects from below. Figure 4(c) shows the radial velocity distribution in the upper portion of the cylinder. At $\theta = 161^{\circ}$ the flow is still developing, with peak velocities occurring near $\tilde{t} = 14.5$.

Figure 5 shows two radial velocity distributions within the core flow as a function of azimuthal location. The small values of $\tilde{v}$ over the entire azimuthal grid for both early and late times are representative of the core resistance to induced fluid motion. The azimuthal velocity in the boundary layer is many orders of magnitude larger than the radial velocity in the core.

The general picture of the flow field involves three major features: (1) a boundary-layer development near the wall due primarily to downward azimuthal fluid flow near the wall, (2) an induced radial velocity that feeds fluid into the developing boundary layer in the upper and middle azimuthal locations of the cylinder and ejects fluid out of the boundary layer at lower azimuthal locations, and (3) a core region that strongly resists first-order motions and only very slowly forces fluid at lower levels to rise and enter the boundary layer. This is a striking example of a flow in which the principal motion is confined to the boundary layer.

The dimensionless temperature ϕ is shown as a function of radial distance in figure 6 for three different azimuthal locations. Here the thermal boundary layer is less well developed than the velocity layer at a given time. The conduction terms in the energy equation dominate the early development of the thermal boundary layer because of the very low fluid velocities that occur shortly after the cold-wall initial condition is imposed.

The early behavior of wall heat transfer is of principal interest, and figure 7 shows the Nusselt number decay with time for four different azimuthal locations. These results appear to be a valid physical representation of the flow development because the convective terms in the energy equation were found to be negligible when very low fluid velocities are present in the early development. The result is an energy balance that is controlled by conduction out of the fluid to the wall until the velocity field develops. The increasing value of Nusselt number with increasing θ gives a clear picture of the positive upward temperature gradient within the boundary layer. This positive upward gradient also exists in the core fluid, as indicated by figure 8. The early establishment of this upward gradient produces a thermally stable core which tends to resist downward motion. The low velocities calculated for the core flow are, in part, a result of this thermal behavior. Figure 9 shows a plot of $N_{Nu}/N_{Gr}^{1/4}$ as a function of time. The cold fluid entering and residing in the lower portion of the cylinder causes a rapid and nearly linear decay of the dimensionless heat-transfer function. For θ near 90° and up to 180° the function decays less rapidly because of the flow of warm fluid into the boundary layer from the core. At very large times the heat-transfer function must asymptotically approach zero because the fluid gives up all its excess energy to the wall. It is apparent that $c_w = \dfrac{N_{Nu}}{N_{Gr}^{1/4}} \to \infty$ as $\tilde{t} \to 0$ because of the step-function cold wall imposed as an initial condition.

The calculated value of c_w at early times near $\tilde{t} = 0$ is dependent on the radial grid spacing used, as might be expected. A comparison of the effects of grid refinement is shown in figure 10. In figure 10(a) the value of T/T_i as a function of radial distance is shown for three different grid networks, where the radial coordinate grid spacings are

0.02, 0.01, and 0.0067. The azimuthal location θ is 90^{o} and the time $\tilde{t}$ is 2.7. As might be expected, a finer grid network steepens the temperature gradient near the wall. The convergence toward a solution that is independent of grid size is indicated by figure 10. Of interest is the velocity distribution shown in figure 10(b). Here, also, convergence is indicated by the results for the refined grid. The velocity peak for the coarse grid, however, is above the peaks for the finer grids. The velocity distribution near the wall appears to be adjusting itself from an "overshoot" where $\Delta\tilde{r} = 0.02$ to a convergent result as $\Delta\tilde{r}$ becomes smaller. Similar results have been computed for Grashof numbers of 8×10^4 and 7×10^7 for the grid spacings given above.

Case III of table I was computed for a Grashof number of 8.34×10^4. The computational time increases considerably at this relatively low Grashof number. Figure 11(a) shows representative azimuthal velocity distributions for this case. These results for the lower Grashof number can be interpreted as being due to a more viscous fluid flow. At a dimensionless time $\tilde{t}$ of 3.07 the boundary layer is considerably thicker than the comparable boundary layer of case I (fig. 3(a)). Even at the early time of $\tilde{t} = 1.31$ the viscous effects are more pronounced than for the higher Grashof number. Figure 11(b) shows typical radial velocity distributions for the low Grashof number (case III). At $\tilde{t} = 3.07$ the distribution shows the effects of higher viscosity in that the profile is thicker than for the case I solution. Finally, figure 11(c) shows the distribution of the dimensionless temperature function. Again, the more viscous fluid of case III shows a thicker thermal boundary layer than that of case I. All the profiles for case III have a qualitative resemblance to those for case I. The solutions for the Nusselt-Grashof relation at the lower Grashof number are shown in figure 11(d). These curves should be compared with the results shown in figure 9.

The computations for the dimensionless dynamic pressure $\tilde{q}$ indicate that the dynamic pressure gradient makes only a negligible contribution to the momentum balance within the fluid; thus, calculations for $\tilde{q}$ were discontinued. This occurrence is consistent with the results reported by Ostrach in reference 1.

The results of the computations for case II at a Grashof number of 1.3×10^6 are shown in figure 12. The velocity and temperature profiles represent a result that is intermediate to the solutions for case III and case I.

Time-Varying Wall Temperature

In order to compare the numerical solution with the experimental results, it was necessary to use a time-dependent wall temperature as a boundary condition. The experimental wall-temperature decay on the inner face can be described by a solution of the one-dimensional heat-conduction equation. For a wall of thickness x_o initially at a temperature $\Phi(x,0) = 1$, where

$$\Phi = \frac{T_w - T_{xo}}{T_i - T_{xo}} \tag{13}$$

the temperature history at the inner face $x = 0$ is given by

$$\Phi(0,\tilde{t}) = 1 - \sum_{n=0}^{\infty} (-1^n)\left[2 \operatorname{erfc} \frac{(2n+1)x_o}{2\sqrt{kx_o\tilde{t}}}\left(\frac{g\beta\alpha}{r_w}\right)^{1/4}(\rho c)^{1/2}\right] \tag{14}$$

With the solution to equation (14) the time dependence of the coefficient $N_{Gr}^{-1/2}$ that appears in equations (1) and (4) may be calculated:

$$\frac{1}{\sqrt{N_{Gr}}} = \frac{1}{\left(\frac{r_w^3 g}{\nu_i^2}\right)^{1/2}\left(1 - \frac{T_{xo}}{T_i}\right)\left[1 - \Phi(0,\tilde{t})\right]} \tag{15}$$

This value is calculated at each time step, and the difference equations are solved by using each new value of Grashof number which results from the time-varying wall temperature. As an example of the solution given by equation (14), figure 13 shows the time-dependent dimensionless wall-temperature decay. Several different limits on the number of terms taken in the summation of equation (14) showed rapid convergence for values of n greater than about 6.

A fundamental difficulty is encountered when the error function solution given by equation (14) is used. At very early times the function is so close to unity that a near singularity is introduced into equation (15). The difference scheme is limited to small time steps, however, for solution of the momentum and energy equations. The wall-temperature decay obtained from equation (14) is numerically incompatible with the difference scheme and does not provide a usable wall boundary condition. This difficulty can be overcome by approximating equation (14) at early times by linear functions of the form

$$\Phi(0,\tilde{t}) = 0.99 - 0.050\tilde{t} \tag{16}$$

Figure 14 shows the azimuthal velocity distribution for case I when the wall temperature decays according to equation (16) rearranged:

$$T_w = \Phi(0,\tilde{t})\left(T_i - T_{xo}\right) + T_{xo} \tag{17}$$

The solutions for a time-dependent wall temperature exhibit several interesting differences from those for a constant wall temperature. In effect, a boundary condition of a slowly cooled wall produces an early driving force that is quite small. This is

characterized by the time development of the Grashof number. Figure 15 shows a typical time history of the Grashof number for the input values of case I and a wall that follows a temperature history given by equations (16) and (17). The development of the flow field is directly related to the time-dependent Grashof number. The immediate consequence of a slowly cooled wall should appear as a flow that is less fully developed at any given time than the flow for which a step-function change in wall temperature has been imposed. The early behavior should be closely related to a flow field having a lower Grashof number. The boundary-layer development follows the rising Grashof number with a behavior that is different from that for a constant wall temperature. In effect, the driving force increases with time, and thus the flow experiences a longer and more pronounced acceleration.

Figure 16(a) shows typical temperature distributions for the boundary conditions of a time-dependent wall temperature and a constant wall temperature. The details revealed by these curves are physically valid in that the distribution for a constant wall temperature, of necessity, must have a steeper slope near the wall in addition to a thinner thermal boundary layer due to the higher Grashof number at equal values of time. These features are clearly evident in figure 16(a).

A comparison of the distributions for constant and variable wall temperatures at equal values of the Grashof number reveals the fundamental differences between the two cases. Figure 16(b) shows that even for equal values of Grashof number the variable wall temperature still has the effect of producing a more viscous flow throughout the entire time development than the constant wall temperature. A comparison with the results for a constant Grashof number is difficult because of the fundamental difference between the two case histories. When the two boundary-layer thicknesses are compared at equal values of $\tilde{r}$ and time, the results shown in figure 17(a) are obtained. The difference in the peak values of the dimensional velocity is of course even greater than that shown in this figure because of the different value of reference velocity used in the nondimensionalization, that is, $u = \sqrt{g\beta\alpha r_w}\,\tilde{u}$. A comparison of the dimensionless azimuthal velocity distributions at equal values of both Grashof number and time is shown in figure 17(b). As expected, the distribution for the time-varying wall temperature shows a thicker profile but a lower peak velocity. Similar results were observed for the temperature distribution, which is also an indirect result of the viscous behavior of the fluid.

Perhaps the most significant single consideration regarding the energy transfer to the walls is the time-dependent Nusselt-Grashof correlation. Hellums (ref. 4) established a constant in the relation $N_{Nu} = c_w N_{Gr}^{1/4}$. For one particular steady flow within a horizontal cylinder, $c_w = 0.326$. If a fully developed flow occurs in the present problem, the time-dependent values of $c_w(\tilde{t})$ should approach the steady value prior to a decay in

the fluid motion. As time increases indefinitely in the present unsteady flow, $c_w(\tilde{t}) \to 0$. The fluid will then have given up all its excess energy to the cold walls. Figure 18 shows the time-dependent behavior for the Nusselt-Grashof correlation. The relation $N_{Nu}/N_{Gr}^{1/4}$ is seen to approach the steady-state value within 1 second $(\tilde{t} = 2.8)$ after flow initiation. The unsteady-flow value of this relation for the present problem must be asymptotic with zero at large values of time. This behavior is implied by the numerical results represented in figure 18.

Figure 19 illustrates the time history of "fluid particles" within the flow field by a sequence of photographs that were taken from an oscilloscope display of the particle displacements computed from the numerical solutions. As shown in these figures, particles were located along rays separated by an azimuthal distance of $\pi/8$ at $t = 0$. From $\tilde{r} = 0$ to $\tilde{r} = 0.64$ the radial spacing between particles $\Delta\tilde{r}$ was 0.04. From $\tilde{r} = 0.64$ to $\tilde{r} = 1.0$ the radial spacing $\Delta\tilde{r}$ was 0.01. A two-dimensional interpolation was used to obtain particle displacements between grid locations for the 31 by 101 mesh in these calculations. The time-dependent wall-temperature decay for case I of table I was used. The sequence of photographs shows the fluid deceleration and stratification near the bottom of the cylinder. Regions in which the number of particles increase represent higher fluid density, as might be expected. Figure 19(c) is a plot of the displacements at 6.6 seconds. In this figure the particles belonging to each original ray have been faired in to illustrate the displacement profiles. Real-time motion pictures were made from plots such as these to give a physical picture of the flow-field development. Because of the low velocities within the core flow, large values of time must be obtained with the numerical solutions before substantial particle displacements can be observed within the core.

EXPERIMENTAL APPARATUS AND PROCEDURE

The instrumented stainless-steel cylinder used for measuring temperature distributions in the gravitationally driven flow field is shown in figure 20. Experiments were made with the cylinder in a horizontal position, with rotation of the cylinder allowed in order to position the thermocouple probes at different locations. The inside diameter of the cylinder was 15.1 cm and the wall thickness was 0.64 cm. The cylinder was 152 cm in length with stainless-steel caps welded on each end. An optical transit was used to provide precise orientation of the cylinder with respect to the Earth's gravitational field vector. Eighteen thermocouple probes were installed over the entire length of the cylinder to provide checks on any end-wall effects that might violate the assumption of two-dimensional flow. Measurable end-wall effects, signifying three-dimensional flow, extended less than 2 cylinder diameters from each end wall. The cylinder was also instrumented with a series of 30-gage copper-constantan thermocouple probes spaced at

$\ell/d = 5$ to allow temperature measurements to be made across the boundary layer and into the core. The probes were installed as shown in figure 21 with the intent of introducing a minimum of disturbance to the flow passing over the probe sensor regions. At large times the probes could affect the flow recirculating from the core into the boundary layer, but the very low fluid velocities and core stratification found in the numerical solutions indicated that such disturbances should be negligible. The errors associated with conduction, radiation, thermal lag, and velocity losses were investigated in reference 8. There it was found that for the test conditions reported, the radiation and thermal-lag errors are significant, whereas conduction and velocity errors remain negligible.

The outer jacket surrounding the cylinder, the hoppers, and the manifold system are shown schematically in figure 22. The 2.54-cm-thick Micarta rings at the bottom of the hoppers served to insulate the outer jacket from the cold liquid being stored in the hoppers. At time zero the plug valves were opened manually and the liquid in the hoppers was dumped around the cylinder walls. The dumping typically took less than 1 second. It was not possible to provide a step-function input to the inner cylinder wall because of the finite thickness of the wall. As mentioned in the previous section, the one-dimensional heat-conduction equation was applicable to a description of the decay of the inner-wall temperature. Once the cold liquid was discharged from the hoppers onto the cylinder wall, a circulation pump was activated to destroy temperature gradients in the cold liquid. In particular, a thermal boundary layer is established between the cylinder wall and the liquid, and this would preclude an accurate prediction of the inner-wall temperature history.

Considerable care was taken in locating the boundary-layer thermocouple probes. These fine wires were quite easily displaced from a fixed position, so that after locating each wire in the correct position, no further instruments or probes were inserted inside the cylinder. Also, charging and purging of dry air in the cylinder were done at a slow rate, so that convection velocities remained below 61 cm/sec at all times. After the test gas was introduced into the cylinder, a waiting period of 2 hours followed to insure that all motion had damped out within the cylinder. From the junction box the signals were transferred to an analog-to-digital data recording system and then read out on computer tape.

One method for varying the Grashof number from one test to another was accomplished by changing the pressure within the cylinder. Each test was repeated a minimum of three times, and calibrated pressure transducers were used to monitor the overall tank pressure during each test. The transducers had a ± 5-percent error limitation, but for all duplicate tests they showed a repeatability better than 5 percent. The coolant temperature was monitored by a thermocouple located in the annular space between the manifold and cylinder wall. The temperature of the outer cylinder wall was also

monitored with a thermocouple installed on the surface. The experimental data reported here were obtained under conditions that produced a minimum ratio of wall temperature to gas temperature $\left(\left(\frac{T_w}{T_i}\right)_{min} = 0.936\right)$ when a nearly steady wall temperature had been achieved after the application of the initial condition.

COMPARISON OF NUMERICAL AND EXPERIMENTAL RESULTS

Comparison of the numerical and experimental results necessitated a consistent formulation of the dimensionless variables as well as identical wall boundary conditions. Also, the numerical solutions must have the initial conditions imposed at the same time zero that actually occurred in the experiments. It was found that within 0.4 second after application of the cold liquid to the cylinder wall, temperature drops were detected within the gas near the wall. Thus, time zero could be determined within 0.4 second by thermocouple signals alone. For comparison with the numerical results the heat-conduction equation was used to determine time zero for the experiments by allowing time zero for the conduction problem to occur when the liquid was first dumped from the hoppers. Time zero for the numerical computations and the fluid was taken when a 0.11K decrease in wall temperature had occurred as a result of conduction.

The foregoing considerations were used to obtain the measured and computed temperature distributions for an azimuthal angle of 90° shown in figure 23. These results correspond to case I of table I with the exception of a variable wall temperature, as mentioned above. The numerical solutions for 1.2, 4.0, and 8.0 seconds of real time compare favorably with the measured results. The large computing time required for the program prohibited carrying out the numerical solutions to larger values of time. The gradual thickening of the thermal boundary layer is seen in figures 23(a) to 23(c). Because the core acts as a reservoir of warm fluid for supplying the boundary layer, the temperature distributions within the layer tend to retain their profiles over a long period of time after the velocity field starts decaying.

To illustrate the temperature decay, figure 24 shows typical plots of both the experimental and theoretical temperature at selected azimuthal locations and at the closest radial location to the wall. The thermal behavior shown in figure 24(a) clearly indicates the inflection produced by the flow as the velocity distribution shifts toward a more developed profile. Similar behavior is seen in figure 24(b) at $\theta = 70^{\circ}$. Finally, at the bottom of the cylinder, where the azimuthal motion of the fluid ceases, the temperature decay shown in figure 24(c) appears.

The numerical results predict a more rapid decay than was actually measured. Several reasons for this discrepancy are possible. The most likely source of error lies

within the framework of the differencing scheme near the midplane of symmetry. Because both the azimuthal and radial velocities are negative near the bottom of the cylinder, forward differencing is used throughout the momentum and energy equations. But forward differencing carries the finite-difference calculations into regions of largest change and tends not to balance with the backward grid points that for the present physical system lie in regions of lesser change. Near the midplane the azimuthal velocity goes to zero, but forward differencing tends to override this, partly because of the finite grid size; thus it appears that errors may be largest near the bottom midplane of symmetry. In this respect the solutions are dependent upon the cylindrical geometry being considered. This dependence represents a limitation, or at least an undesirable aspect, of one-sided finite-difference techniques.

It is of some interest to observe the experimentally measured pressure decay within the cylinder. This decay represents a three-dimensional (closed-volume) phenomenon which is in a sense primarily dependent on the two-dimensional flow field that transports heat to the cylinder walls. Figure 25 shows a typical measured and calculated pressure decay for a maximum Grashof number of 7×10^7 (case I). The pressure decay is a direct measure of the overall energy loss from the fluid. The average density in the enclosed cylinder remains constant, and thus values of the average tank pressure are directly proportional to the average fluid temperature within the cylinder.

The single most useful comparison made between the numerical results and the experiments is that of the Nusselt-Grashof relation for the time-dependent flow. Figure 26 shows the measured time-dependent variation of this dimensionless quantity. The comparison is favorable. The Nusselt-Grashof relation approaches the steady-state value within 4 seconds $(\tilde{t} = 10)$ after flow initiation and is asymptotic with zero at large values of time.

If figure 26 is compared with figure 18, the effect of a steadily decaying wall temperature is apparent. The curve shown in figure 26 results because lower values of heat transfer occur when the wall is cooled unsteadily than when a step-function cold wall is applied, such as in the conditions for figure 18.

Examples of typical experimental radial temperature distributions are shown in figure 27. In figure 27(a) at $t = 4.0$ seconds, the wall has cooled to about 0.983 of the initial temperature, and thus the distribution terminates at the wall $(\tilde{r} = 1.0)$ in the manner shown.

The thermocouple located at $\tilde{r} = 0.2$ was considered essential for monitoring the core temperature. If a very low ratio of T_w/T_i had been utilized, it could be anticipated that fluid would fall downward from the uppermost walls of the cylinder. In such a case a negative vertical temperature distribution within the core might have been observed. For the value of T_w/T_i of these experiments the flow was almost completely confined

within the wall boundary layers, and no negative upward distributions were measured. Figure 27(b) shows the temperature distribution at 8.0 seconds after flow initiation. The measured profile has broadened more than the numerical solutions predict. The agreement is reasonable, however, considering the high degree of nonlinearity of the problem when the walls are cooled unsteadily. Figures 28(a) and 28(b) show a similar result for $\theta = 70^{\circ}$.

A series of experiments at Grashof numbers up to about 6.5×10^5 were made, and some results are shown in figure 29. The very slow time development of the flow field is indicated both by the numerical calculations, which take a computational time almost an order of magnitude longer than the case I solution, and by the experiments. The agreement between the numerical solutions and the experiments is not as good as that for the results at the higher Grashof number. The very slow development of the flow reduces the accuracy at early times because of the small differences in temperature that must be measured. Figure 30 is a plot of the time history of the boundary-layer temperature at $\tilde{r} = 0.966$. The slow decay is an example of the behavior at the lower Grashof number. However, the more rapid reduction of the ratio of gas temperature to wall temperature for the lower Grashof number produces an undershoot of the Nusselt-Grashof relation. This is due to the differences between the velocity-field development and the thermal-field development and is shown in figure 31. An initial response to the near singularity at early times due to low values of the Grashof number causes the undershoot in the numerical results. Thus, although the disturbance is damped by the difference scheme, the accuracy of the results is severely lessened by the destabilizing influence of a very low Grashof number at early times. Restated, the computations for the low Grashof number are characterized by a relatively rapid wall cooling which raises the wall heat transfer more rapidly than the one-fourth power of the Grashof number. The Nusselt-Grashof behavior in both figures 26 and 31 must be viewed as being representative of one specific flow configuration and also a very specific boundary condition. The difference between the results shown in figures 26 and 31 indicates that a single correlation equation from the numerical results presented here may not be possible to achieve for the entire range of unsteady laminar natural convection within a horizontal cylinder.

CONCLUDING REMARKS

The present investigation has revealed the dynamic and thermal behavior of a confined fluid subjected to gravitational body forces. For an infinite horizontal cylinder with uniformly cold walls imposed as an initial condition, the principal features of the flow involve a rapid development of the boundary layer adjacent to the walls, a tendency for fluid stratification in the lower regions of the cylinder, and a slow decay of the velocity and thermal fields with time. Experiments made in this investigation substantiate the

thermal behavior predicted by numerical solutions to the quasi-compressible Navier-Stokes equations for a time-dependent wall-temperature decay. Because the thermal and velocity fields are strongly coupled, the experimental findings imply that the velocity field may also be accurately described by the numerical results. The following remarks can be made from this study:

The relationship between the Nusselt and Grashof numbers is found both numerically and experimentally for unsteady natural convection within a horizontal cylinder subjected to uniformly cold walls as boundary conditions. For the condition of a constant cold wall from time zero, the numerical results show that the Nusselt-Grashof relation approaches the steady-state value about 1 second after commencement of the flow down the cylinder wall. For the boundary condition of a time-dependent wall temperature, the Nusselt-Grashof relation approaches the steady-state value about 4 seconds after the commencement of flow down the cylinder walls.

The combination of early establishment of a positive upward temperature gradient within the central core flow and the effects of fluid viscosity produces a strong resistance to induced fluid motion within the core. After initiation, the flow within the boundary layer develops rapidly, and decays over a long period of time.

The dynamic pressure gradient terms in the Navier-Stokes equations for azimuthal and radial momentum are negligible for the conditions considered in this investigation.

For natural convection with very low velocity, windward finite differencing, which gives first-order accuracy in time and space, is a suitable numerical scheme when positive and negative velocities occur. The large computing time required for such flow fields rules out more complex differencing schemes at the present time.

The differencing scheme appeared to lose accuracy for the flow near the bottom of the cylinder, where both the radial and azimuthal velocities are negative and the azimuthal velocity decelerates to zero at an azimuthal angle of zero.

No first-order motion was found within the core flow. The absence of this motion is attributed to the boundary conditions, which require azimuthal deceleration of the boundary-layer flow near the bottom of the cylinder. Both the theoretical and experimental models establish a midplane of symmetry that satisfies the boundary conditions imposed in this study.

The present studies are applicable strictly to the regime of laminar natural convection. The limit of laminar flow over cylinders in the external flow situation has been observed to occur at Grashof numbers near 3×10^9. For the high-pressure full-scale facility discussed in AIAA Paper No. 71-254, the Grashof number near the end of the charging cycle would be slightly in excess of this value, and turbulent heat-transfer rates could be expected. Experimental steady-state heat-transfer results, however, show only

a slight difference in slope due to the change from laminar to turbulent flow. In addition, the time history of the rate of increase in heat transfer in the full-scale charging cycle would produce a time-dependent Grashof number even for a steady-state wall temperature.

Finally, a full-scale facility could introduce axial flow within the chamber as a result of the method of injection of gas during charging. Only if the axial velocities were much less than the azimuthal velocities induced by a cold-wall boundary condition, would the overall heat transfer be expected to show small differences from the value for a truly two-dimensional flow field.

Langley Research Center,
National Aeronautics and Space Administration,
Hampton, Va., September 24, 1974.

REFERENCES

1. Ostrach, Simon: Laminar Flows With Body Forces. Theory of Laminar Flows, F. K. Moore, ed., Princeton Univ. Press, 1964, pp. 528-718.

2. Menold, Ernest Robert: Natural Convection in a Horizontal Cylinder at Large Prandtl Numbers. Ph. D. Thesis, Case Inst. Technol., 1965.

3. Hantman, Robert G.; and Ostrach, Simon: Natural Convection Inside a Horizontal Circular Cylinder. AFOSR-68-2341, U.S. Air Force, Jan. 1969. (Available from DDC as AD 683 049.)

4. Hellums, Jesse David: Finite Difference Computation of Natural Convection Heat Transfer. Ph. D. Thesis, Univ. of Michigan, 1960.

5. Martini, William R.; and Churchill, Stuart W.: Natural Convection Inside a Horizontal Cylinder. AIChE J., vol. 6, 1960, pp. 251-257.

6. Brooks, Irving H.; and Ostrach, Simon: An Experimental Investigation of Natural Convection in a Horizontal Cylinder. AFOSR-TR-69-0174, U.S. Air Force, Jan. 1969. (Available from DDC as AD 685 176.)

7. Boatright, W. B.; Sabol, A. P.; and Stewart, R. B. (With appendix A by G. M. Stokes and appendix B by W. B. Olstad): Stored Arc-Heated Air – A Concept for a High Reynolds Number, Mach 8 to 10, True Temperature Test Facility. AIAA Paper No. 71-254, Mar. 1971.

8. Stewart, Roger Bell: Numerical and Experimental Studies of The Natural Convection Flow Within a Horizontal Cylinder Subjected to a Uniformly Cold Wall Boundary Condition. Ph. D. Thesis, Virginia Polytech. Inst. and State Univ., Oct. 1972. (Available as NASA TM X-69220.)

9. Hermann, R.: Heat Transfer by Free Convection From Horizontal Cylinders in Diatomic Gases. NACA TM 1366, 1954.

10. Batchelor, G. K.: Heat Transfer by Free Convection Across a Closed Cavity Between Vertical Boundaries at Different Temperatures. Quart. Appl. Math., vol. XII, no. 3, Oct. 1954, pp. 209-233.

11. Pillow, A. F.: The Free Convection Cell in Two Dimensions. Rep. A. 79, Aeronaut. Res. Lab., Australia Dep. Supply, May 1952.

12. Roache, Patrick J.: Computational Fluid Dynamics. Hermosa Publ., c.1972.

13. Callens, E. Eugene, Jr.: A Time-Dependent Approach to Fluid Mechanical Phenomenology. AIAA Paper No. 70-46, Jan. 1970.

TABLE I.- PARAMETER VARIATIONS FOR NUMERICAL STUDIES

Case I:		
Grashof number	7×10^7	0 to 7×10^7
Prandtl number	0.715	0.715
T_w/T_i	0.936	Variable
T_w	Constant	$\Phi(0,\tilde{t})(T_i - T_{xo}) + T_{xo}$
r_w, cm	7.6	7.6
p_i, atm*	6.74	6.74
t, sec	$0.35\tilde{t}$	Variable $\tilde{t}$
Case II:		
Grashof number	1.36×10^6	0 to 1.36×10^6
Prandtl number	0.715	0.715
T_w/T_i	0.936	Variable
T_w	Constant	$\Phi(0,\tilde{t})(T_i - T_{xo}) + T_{xo}$
r_w, cm	7.6	7.6
p_i, atm	1	1
t, sec	$0.35\tilde{t}$	Variable $\tilde{t}$
Case III:		
Grashof number		8.34×10^4
Prandtl number		0.715
T_w/T_i		0.936
T_w		Constant
r_w, cm		3.1
p_i, atm		1
t, sec		$0.22\tilde{t}$

*1 atm = 101.3 kN/m^2.

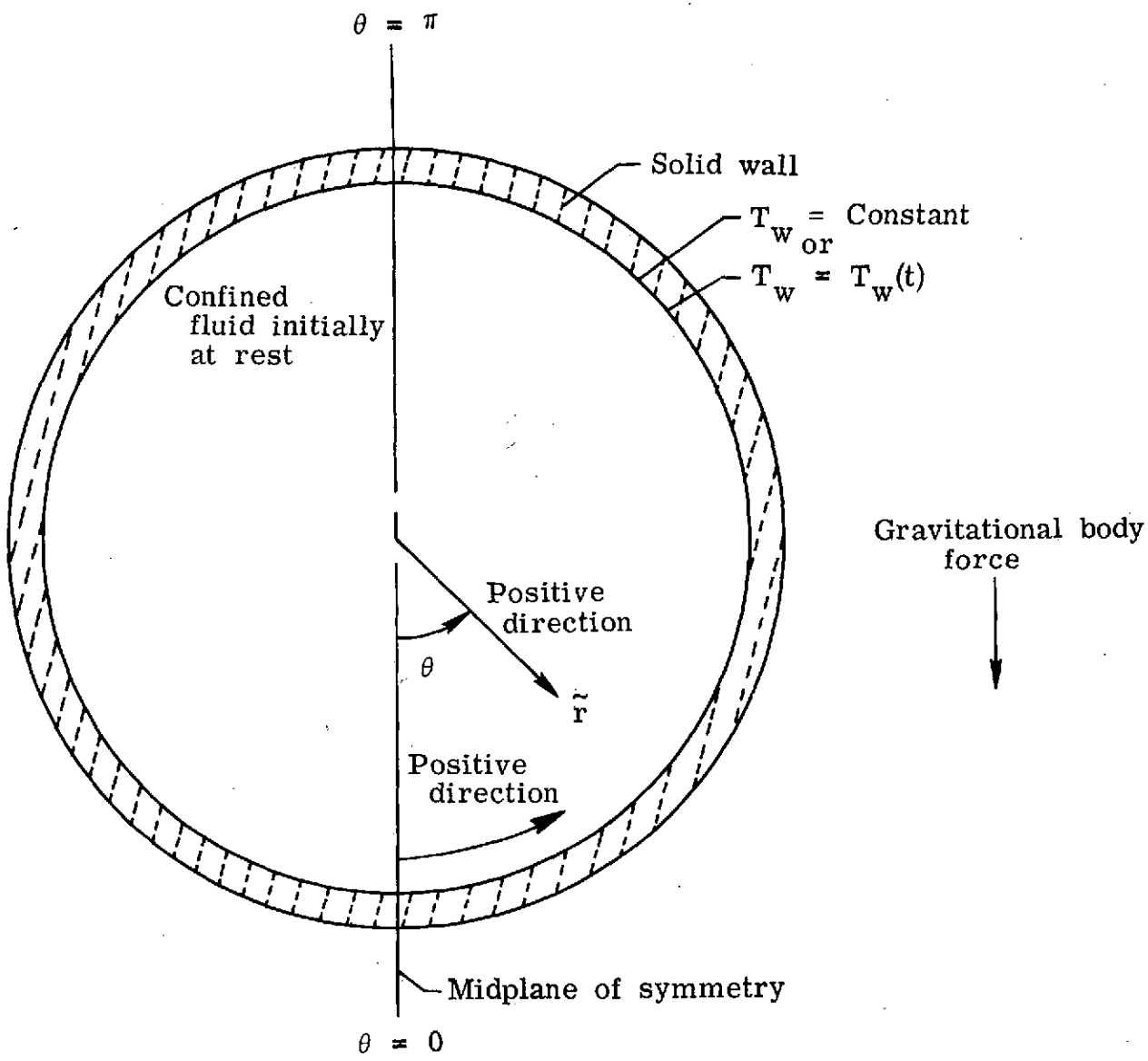

Figure 1.- Geometry of horizontal cylinder.

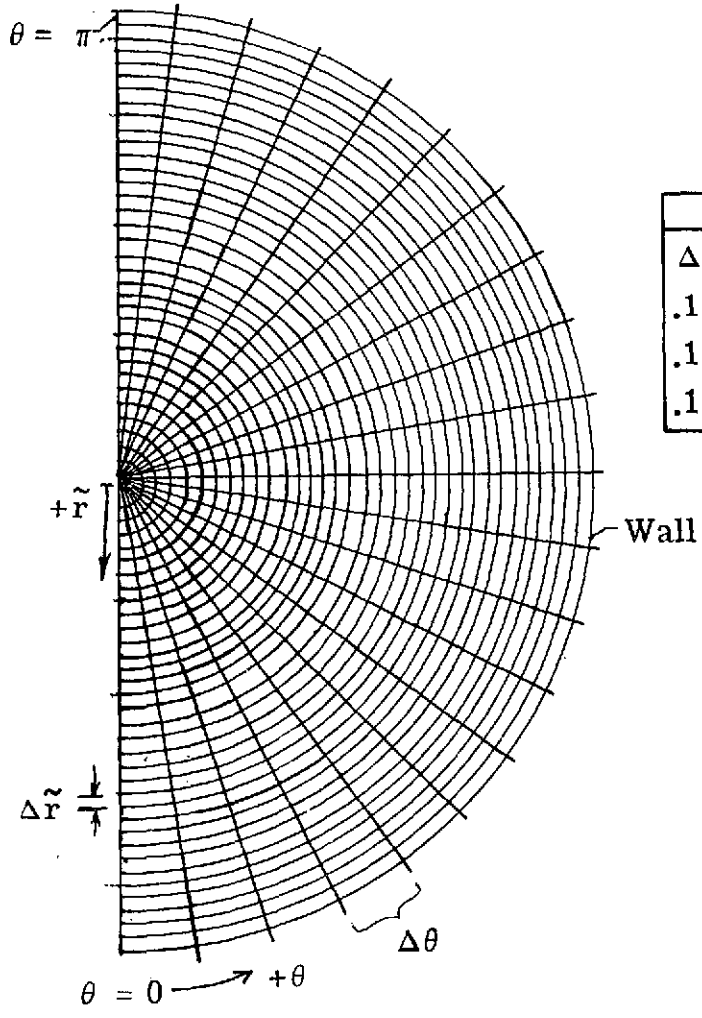

Grid sizes used		
$\Delta\theta$	$\Delta\tilde{r}$	Grid
.108	.0067	31 by 151
.108	.01	31 by 101
.108	.02	31 by 51

Figure 2.- Finite-difference grid network.

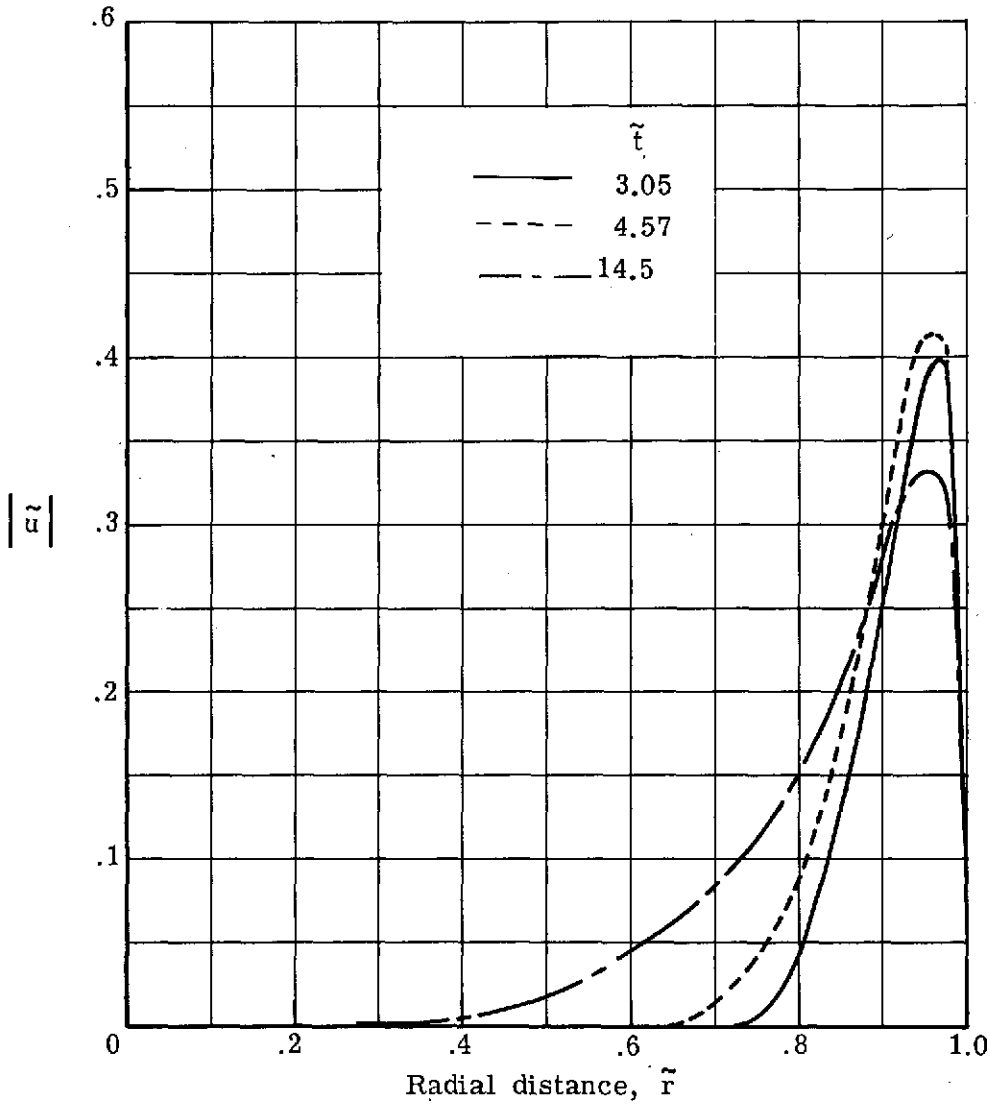

(a) $\theta = 90^{o}$.

Figure 3.- Azimuthal velocity variation with radial distance. Case I; $N_{Gr} = 7 \times 10^{7}$; grid, 31 by 51.

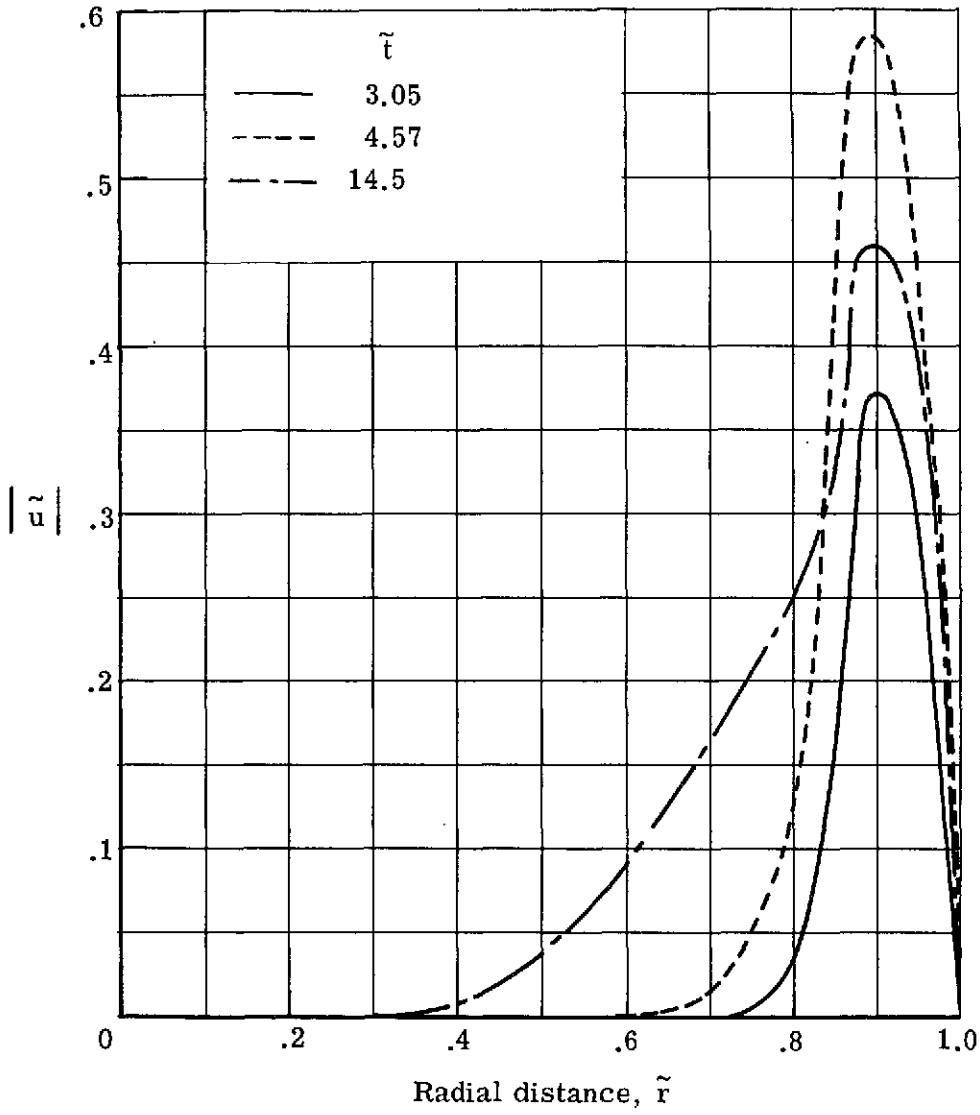

(b) $\theta = 23.7^{o}$.

Figure 3.- Continued.

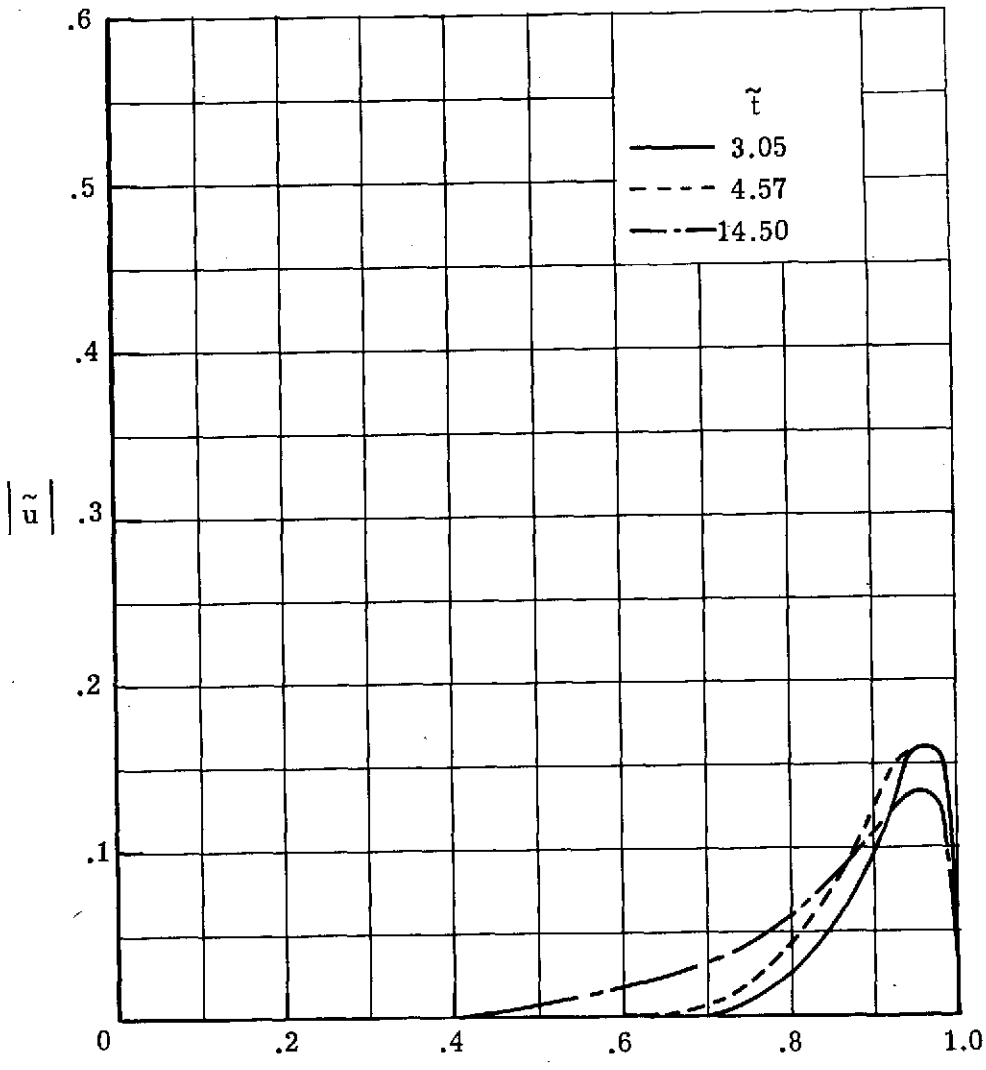

(c) $\theta = 161^{o}$.

Figure 3.- Concluded.

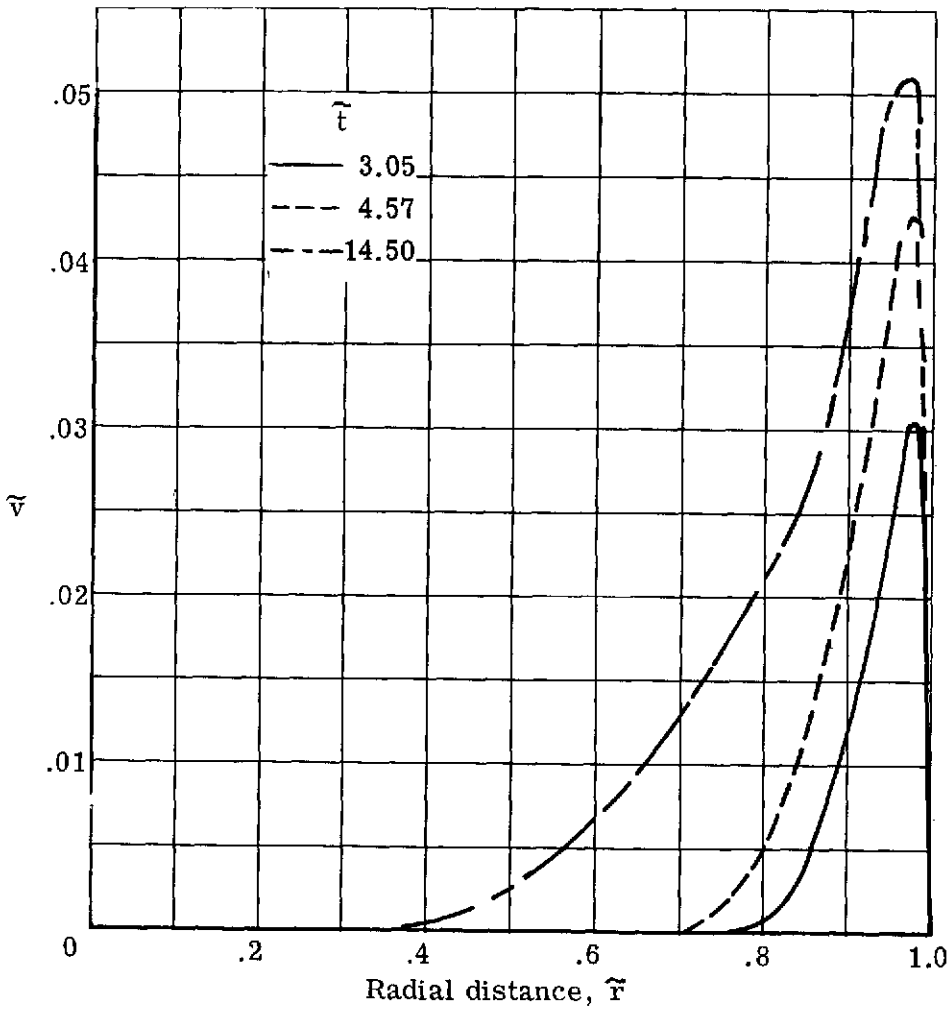

(a) $\theta = 90^{o}$.

Figure 4.- Radial velocity variation with radial distance. Case I; $N_{Gr} = 7 \times 10^{7}$; grid, 31 by 51.

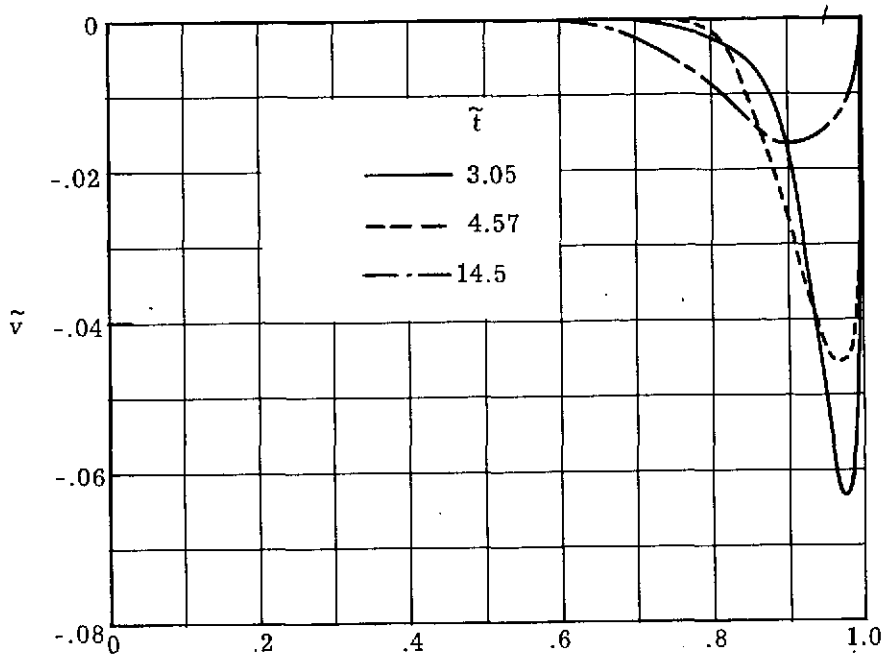

(b) $\theta = 23.7^{\circ}$.

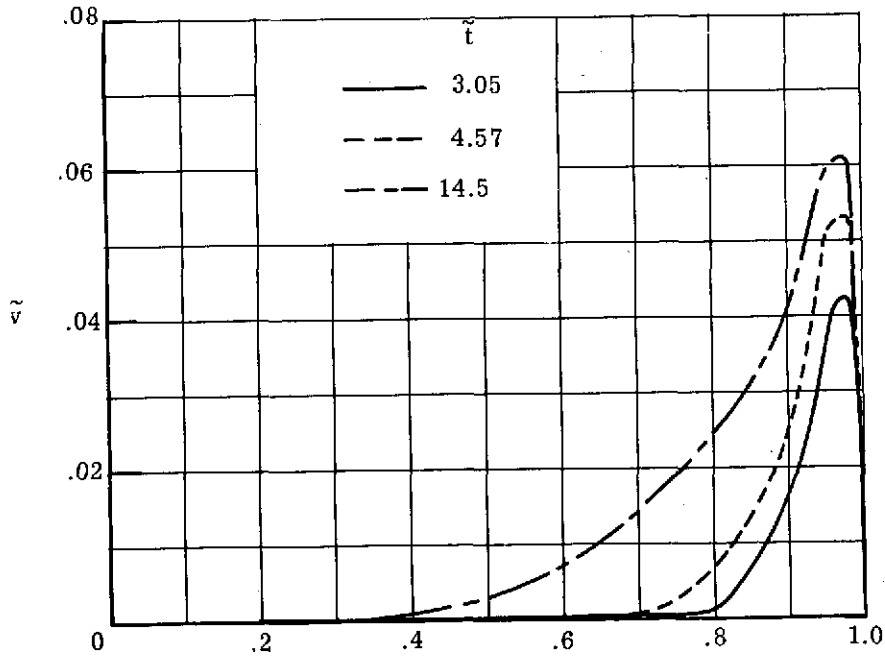

(c) $\theta = 161^{\circ}$.

Figure 4.- Concluded.

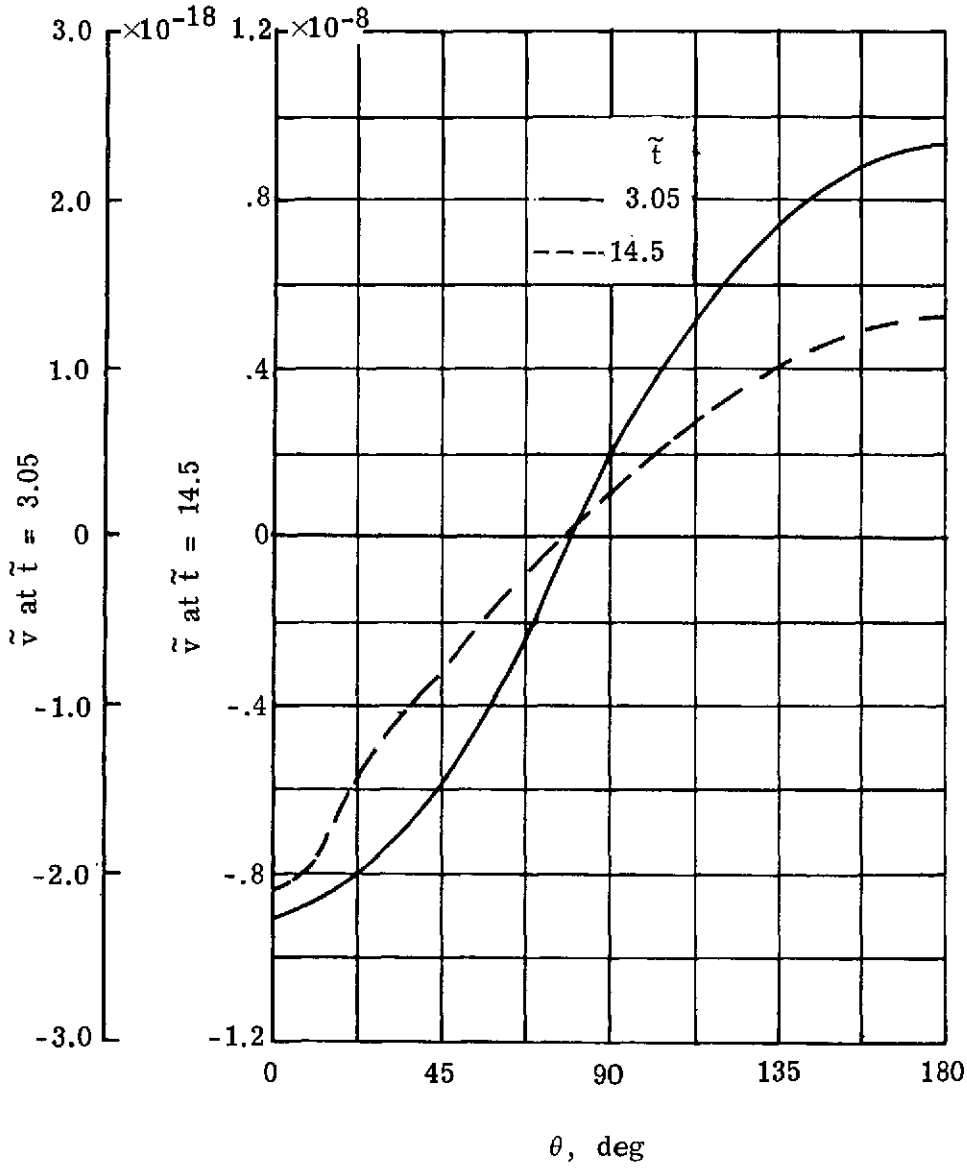

Figure 5.- Radial velocity distribution within the core as a function of azimuthal location. Case I; $N_{Gr} = 7 \times 10^7$; $\tilde{r} = 0.44$.

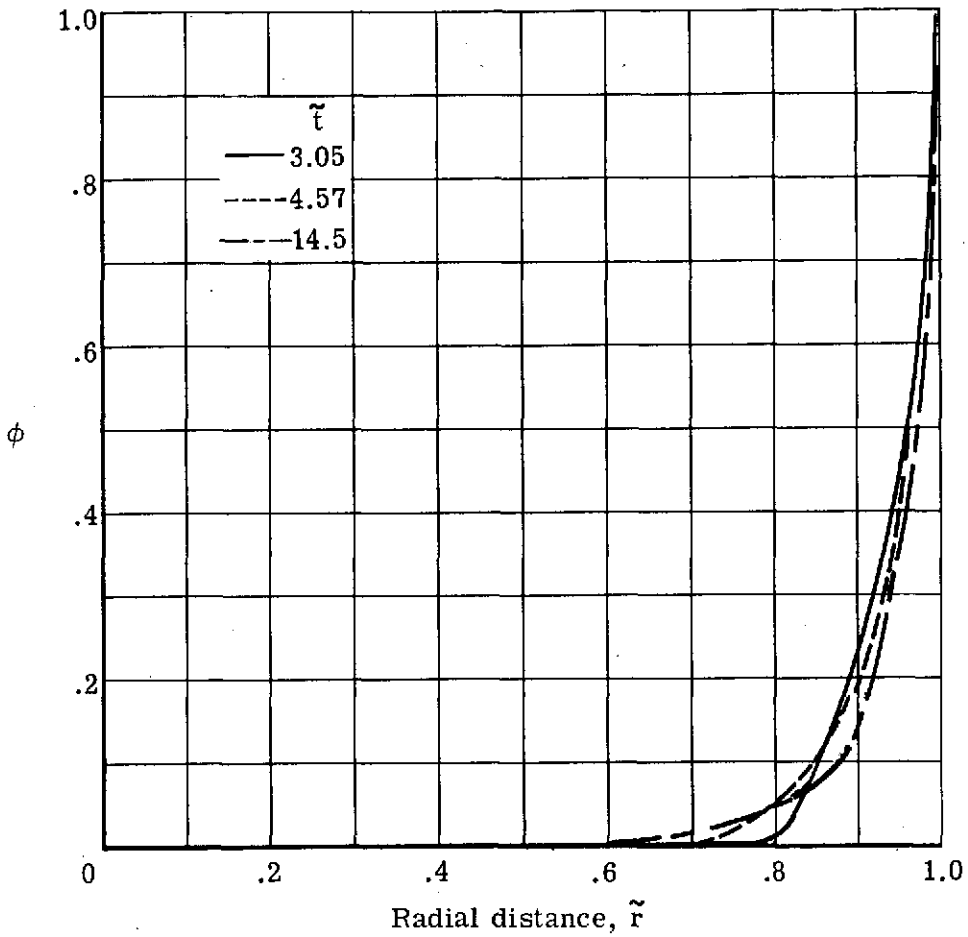

(a) $\theta = 90^{o}$.

Figure 6.- Temperature variation with radial distance. Case I; $N_{Gr} = 7 \times 10^{7}$; grid, 31 by 51.

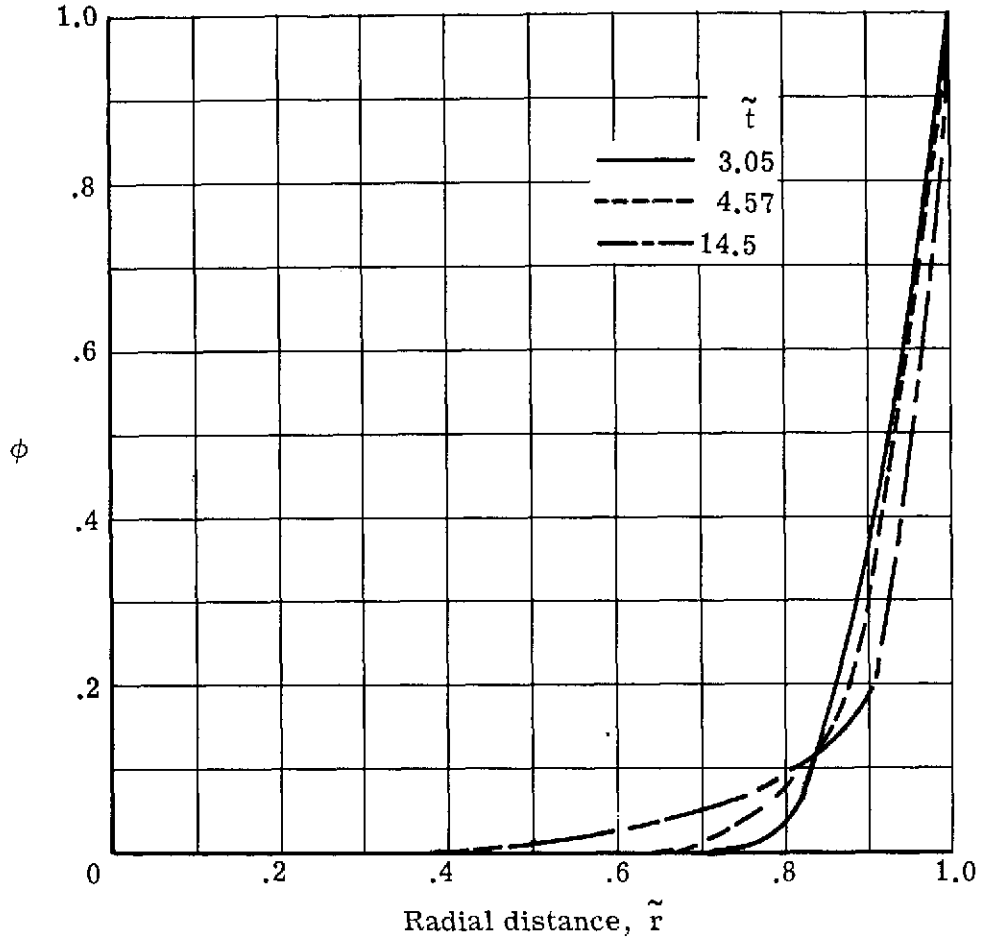

(b) $\theta = 23.7^{o}$.

Figure 6.- Continued.

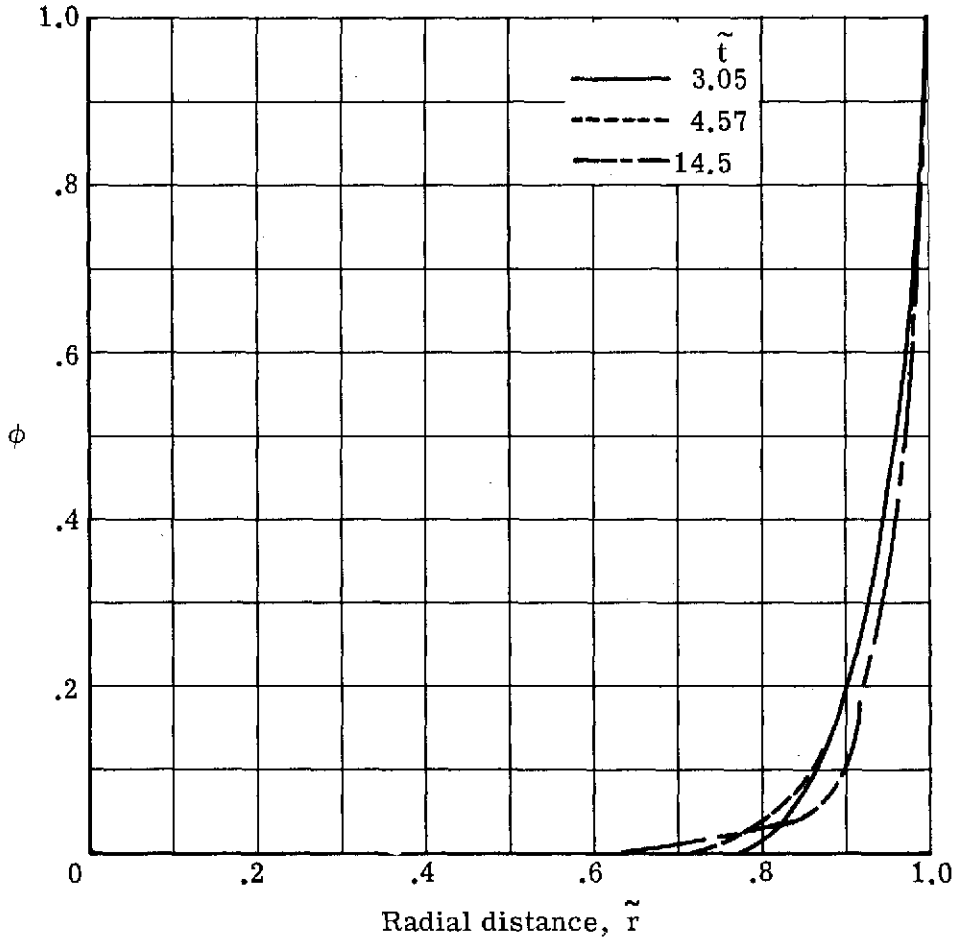

(c) $\theta = 161^{\circ}$.

Figure 6.- Concluded.

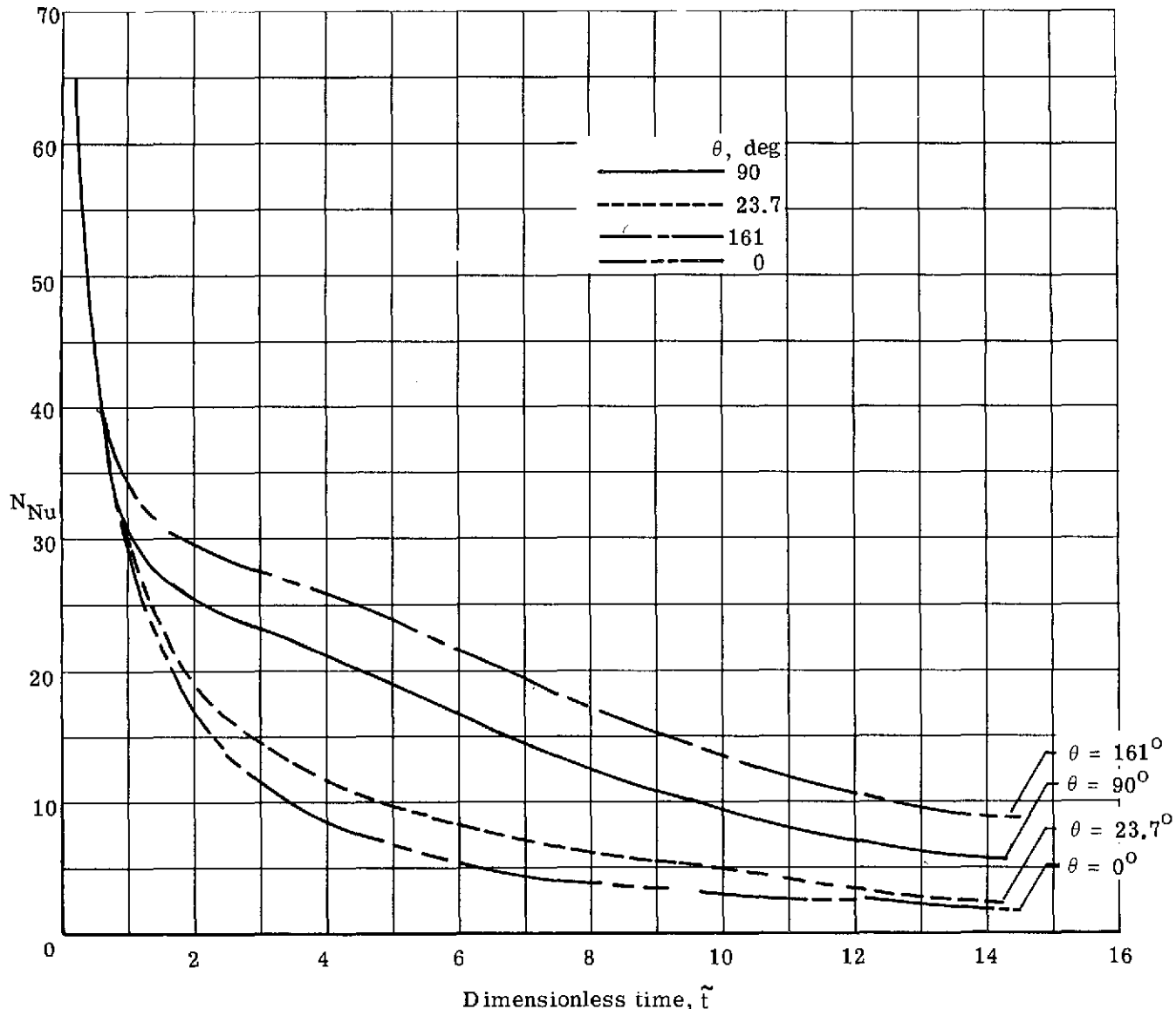

Figure 7.- Nusselt number decay with time. Case I; $N_{Gr} = 7 \times 10^{7}$; grid, 47 by 161.

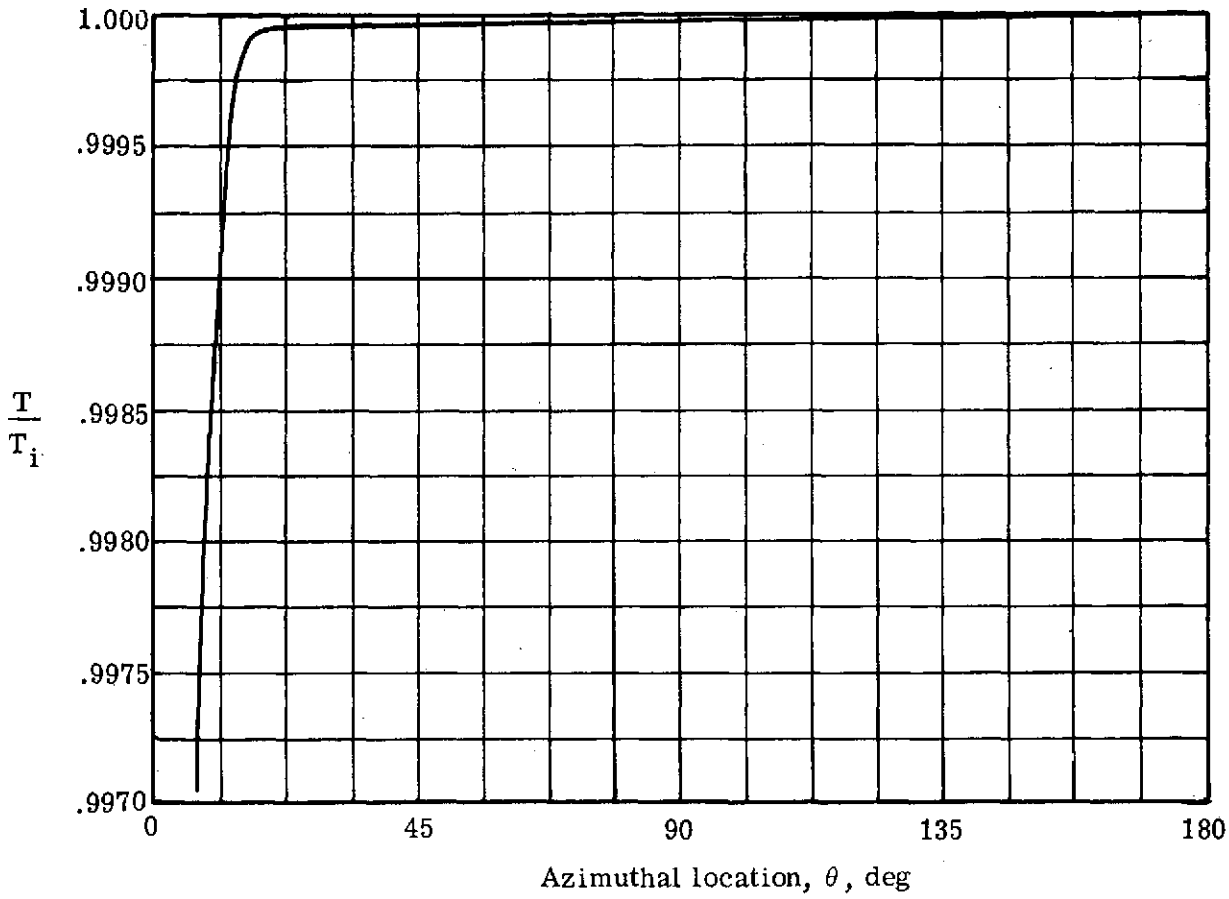

Figure 8.- Azimuthal temperature distribution within the core. Case I; $N_{Gr} = 7 \times 10^7$; $\tilde{t} = 19.1$; $\tilde{r} = 0.44$.

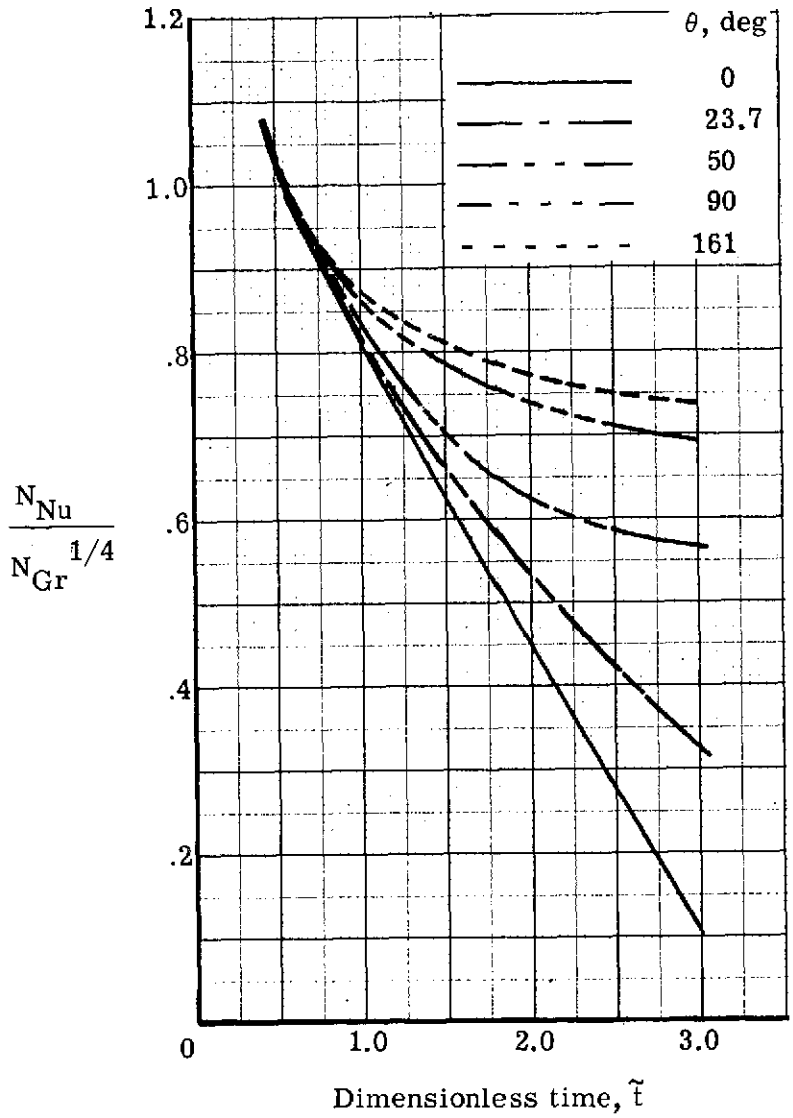

Figure 9.- Nusselt-Grashof relation for time-dependent natural convection. Case I; grid, 31 by 101.

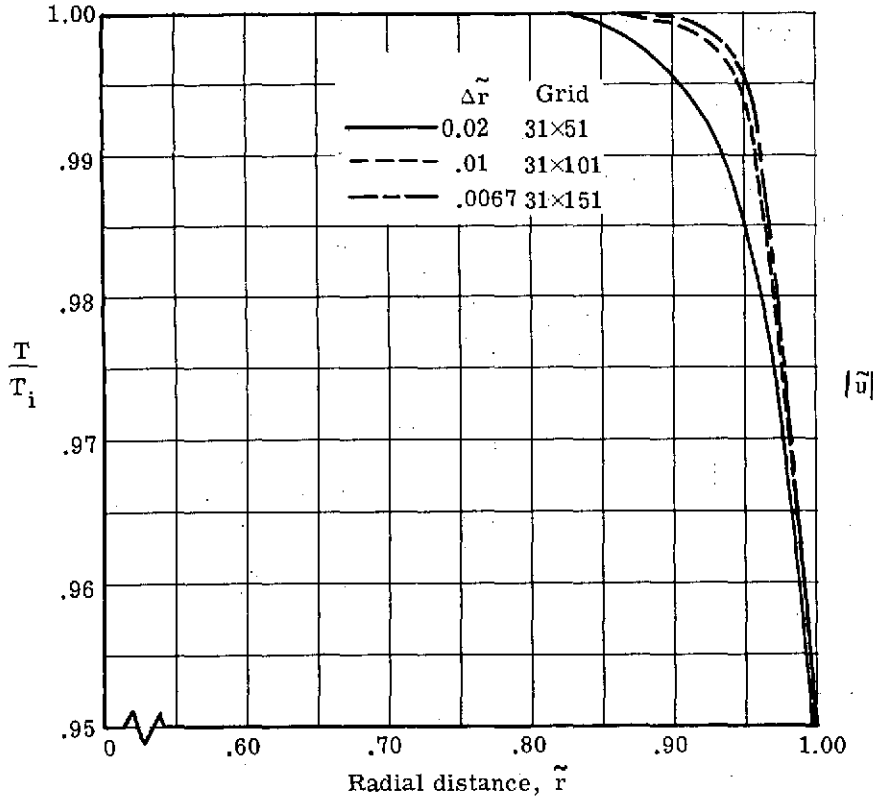

(a) Temperature distribution.

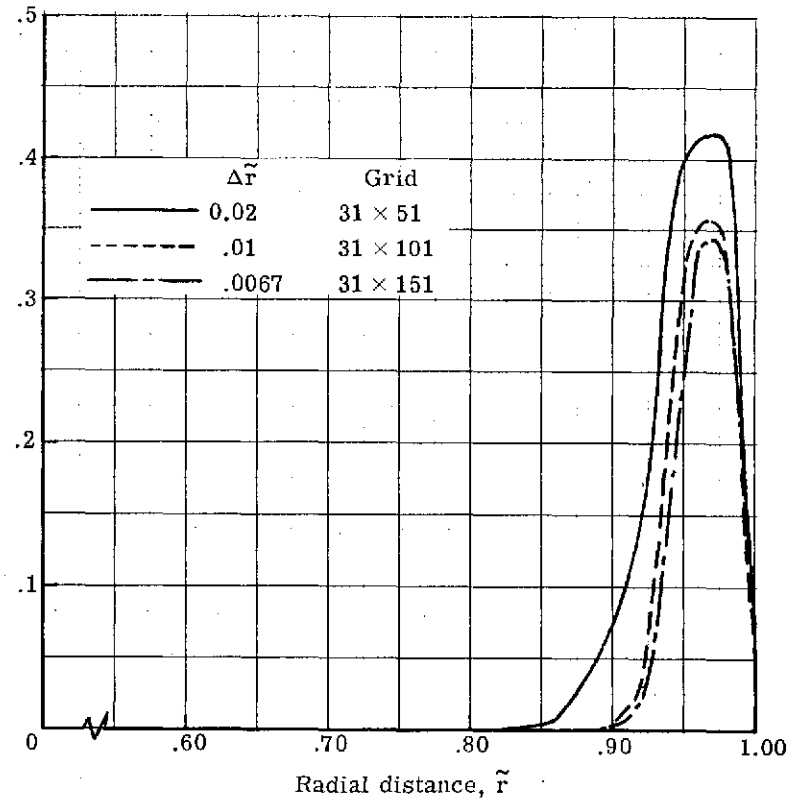

(b) Velocity distribution.

Figure 10.- Effects of radial grid refinement for a Grashof number of 1.36×10^6. Case II; $\tilde{t} = 2.7$.

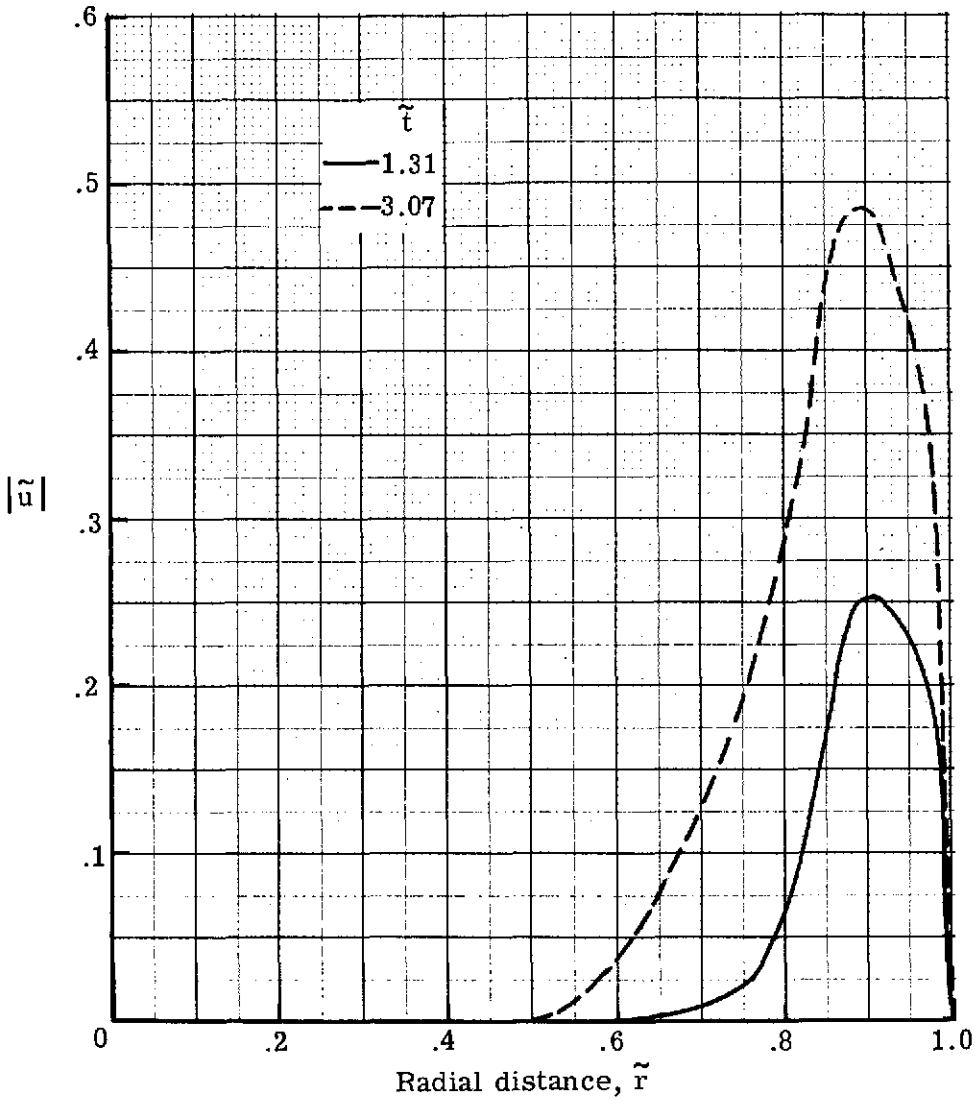

(a) Azimuthal velocity distribution. Case III; $N_{Gr} = 8.34 \times 10^4$; $\theta = 90^o$; grid, 31 by 51.

Figure 11.- Results for natural convection at low Grashof number.

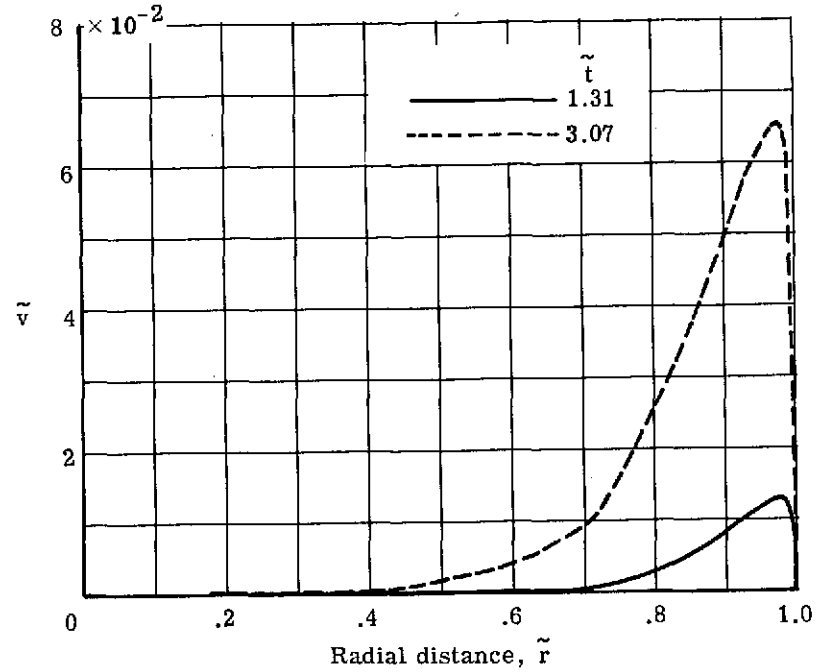

(b) Radial velocity distribution. Case III; $N_{Gr} = 8.34 \times 10^4$; $\theta = 90^o$; grid, 31 by 51.

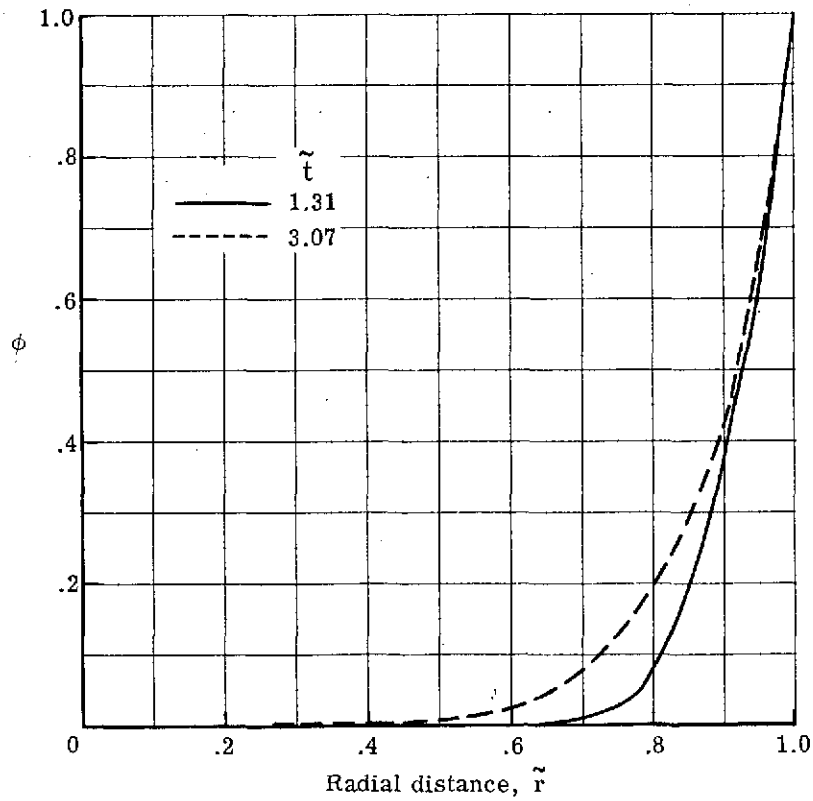

(c) Temperature distribution. Case III; $N_{Gr} = 8.34 \times 10^4$; $\theta = 90^o$; grid, 31 by 51.

Figure 11.- Continued.

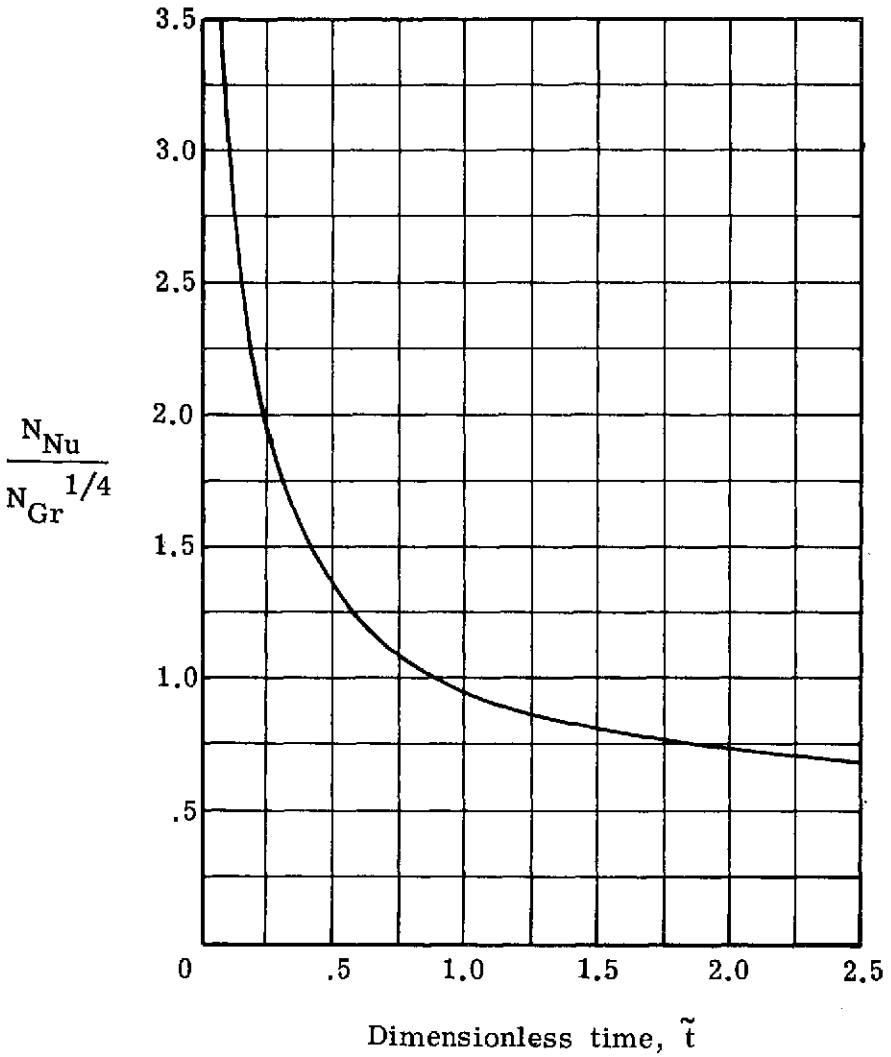

(d) Nusselt-Grashof relation. Case III; $N_{Gr} = 8.34 \times 10^4$; $\frac{T_w}{T_i} = 0.936$.

Figure 11.- Concluded.

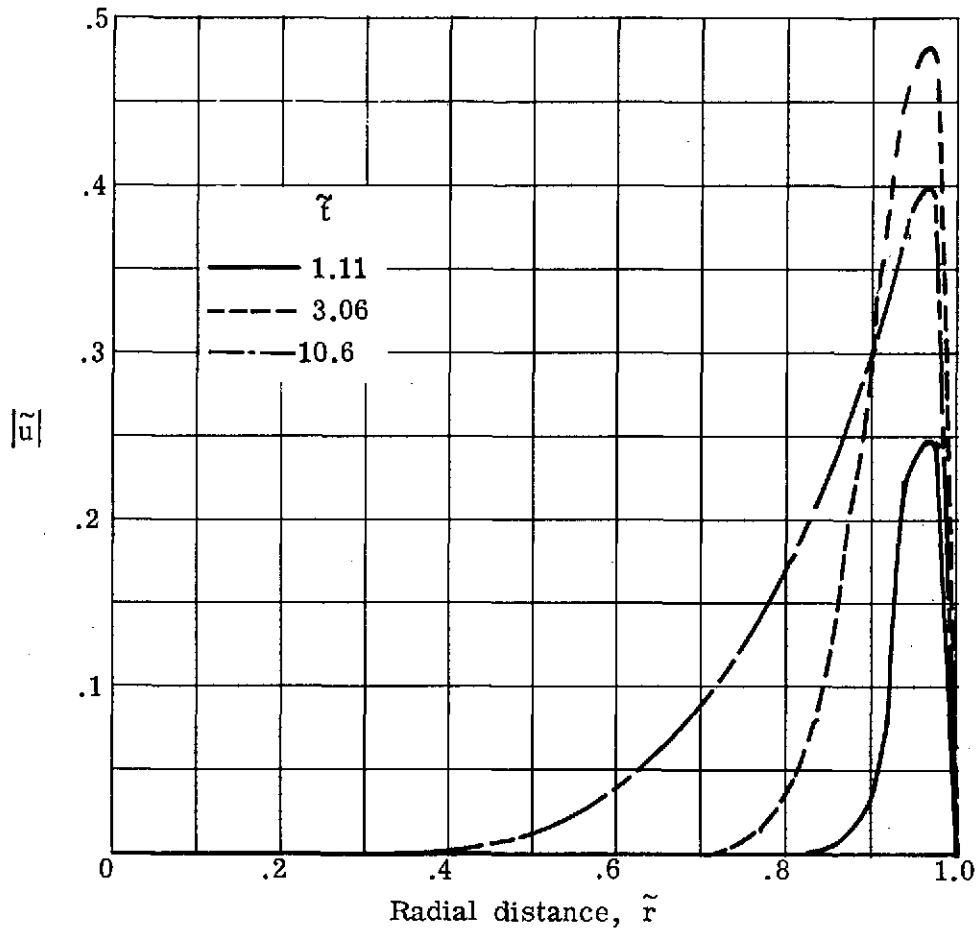

Figure 12.- Azimuthal velocity distribution in horizontal cylinder. Case II; $N_{Gr} = 1.3 \times 10^6$; $\theta = 90^\circ$; grid, 31 by 101.

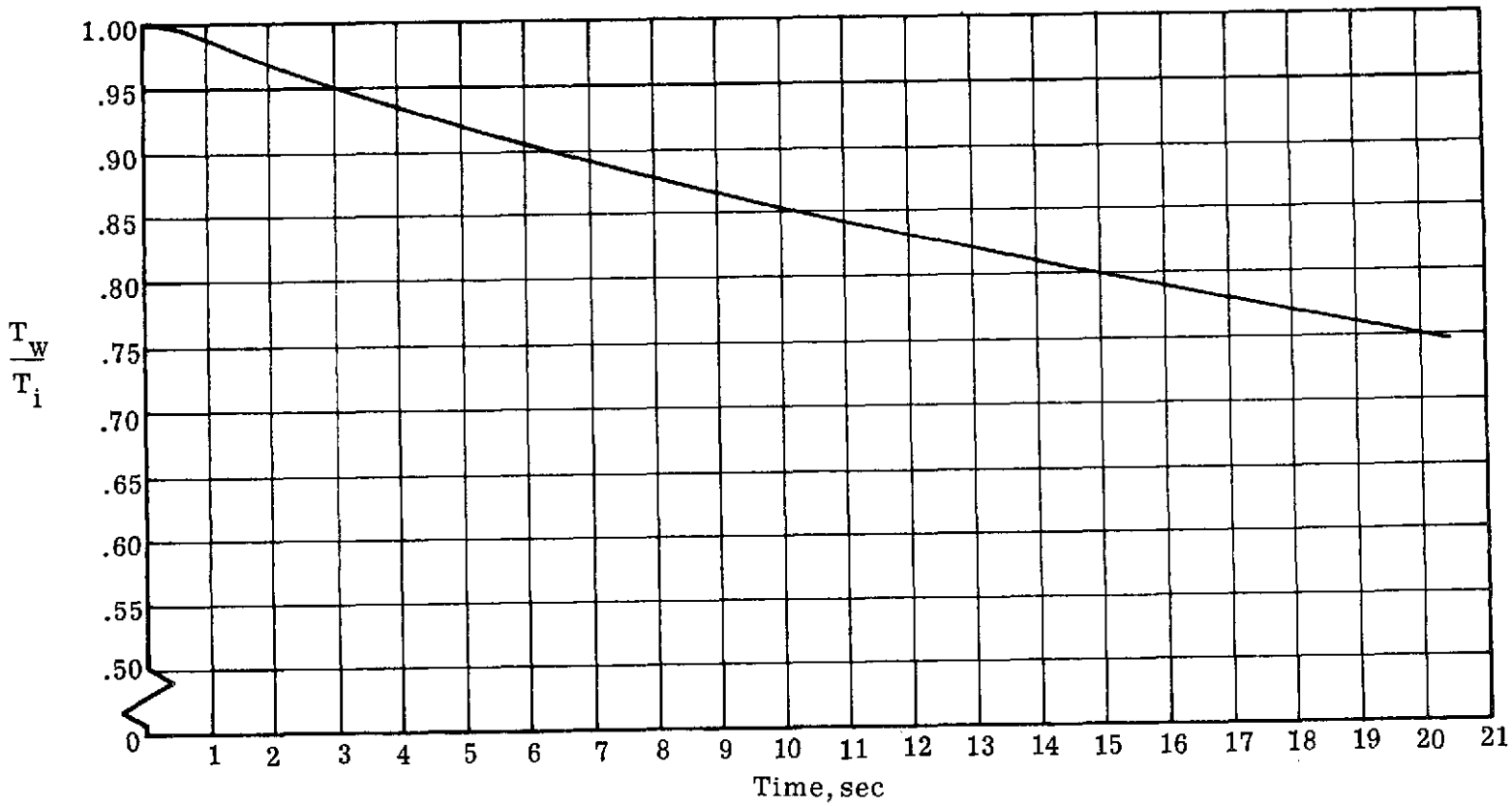

Figure 13.- Wall-temperature decay from the heat-conduction equation.

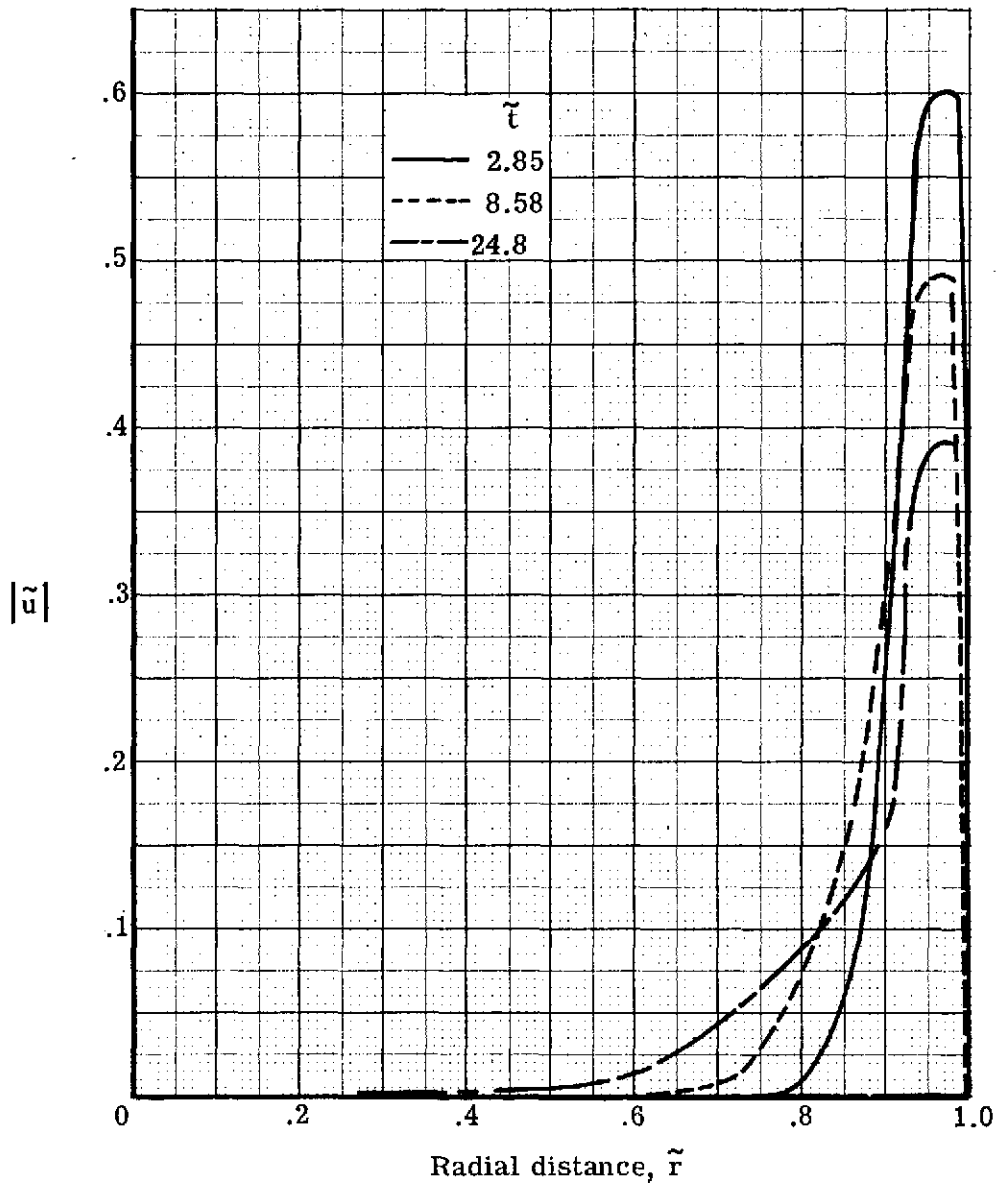

Figure 14.- Azimuthal velocity distribution for time-dependent wall temperature. Case I; $N_{Gr} = 1.36 \times 10^7$; T_w, variable; $\theta = 90^o$.

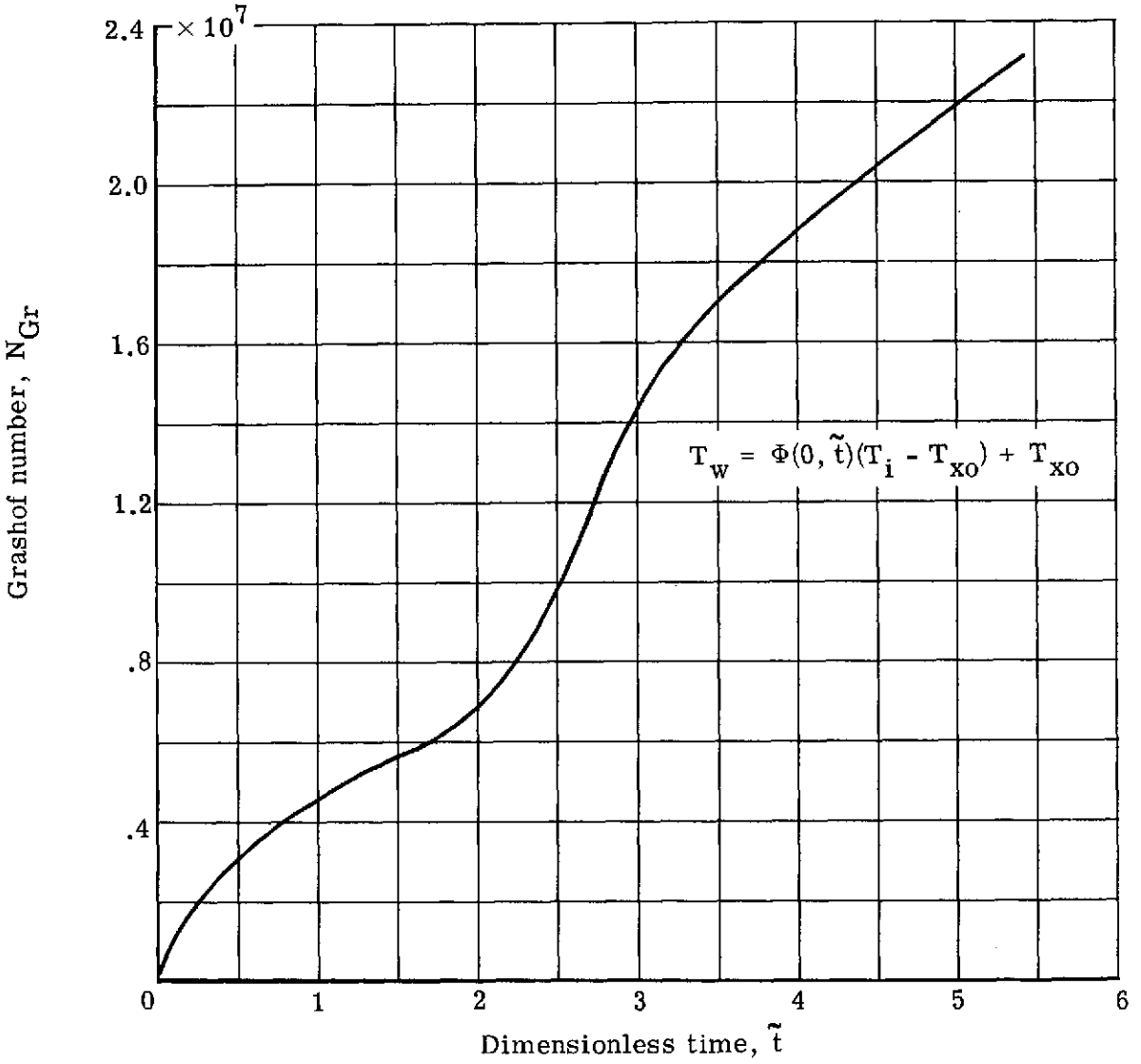

Figure 15.- Time development of the Grashof number for unsteady wall temperature. Case I; grid, 31 by 51.

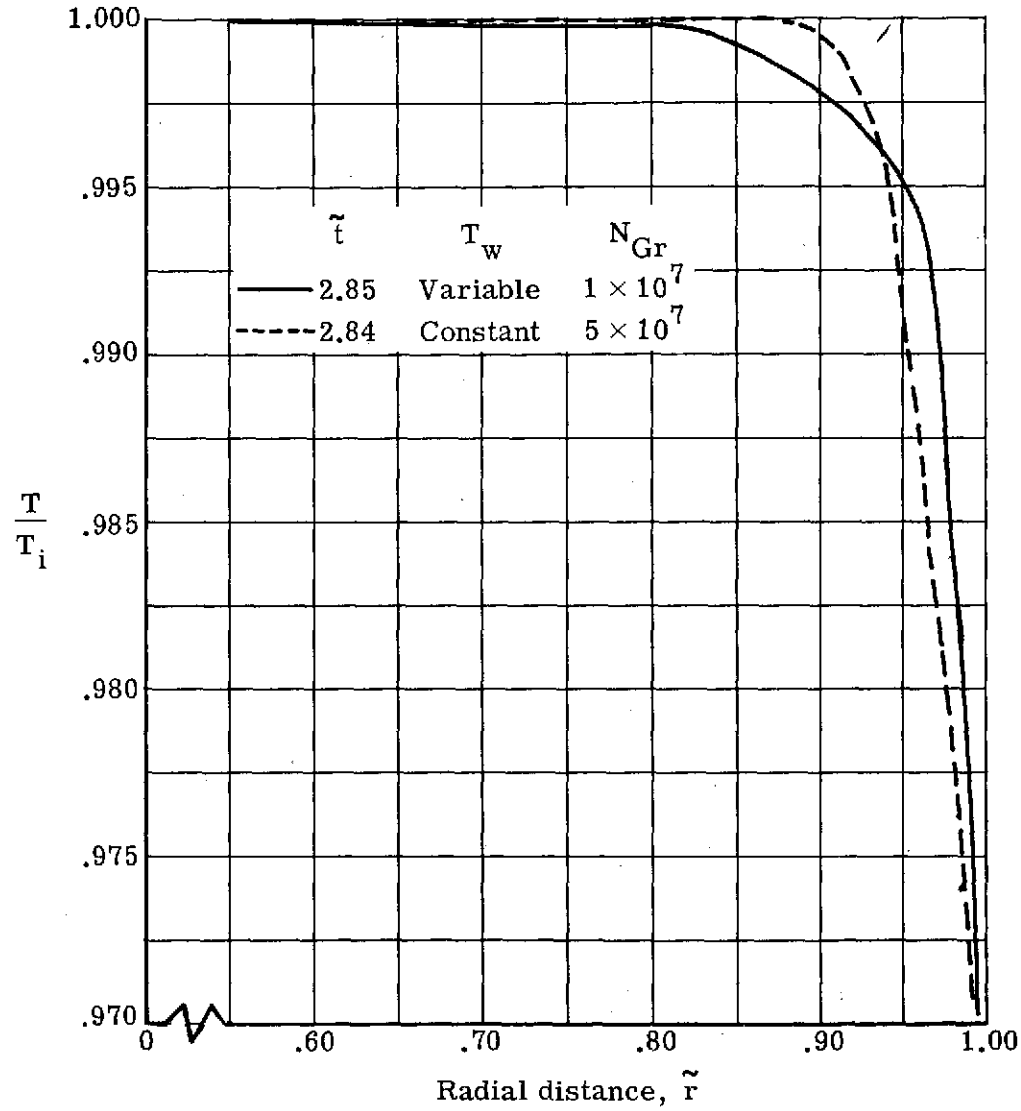

(a) Variable Grashof number.

Figure 16.- Temperature distributions for a constant and a time-dependent wall temperature. Case I; $\theta = 90^{o}$.

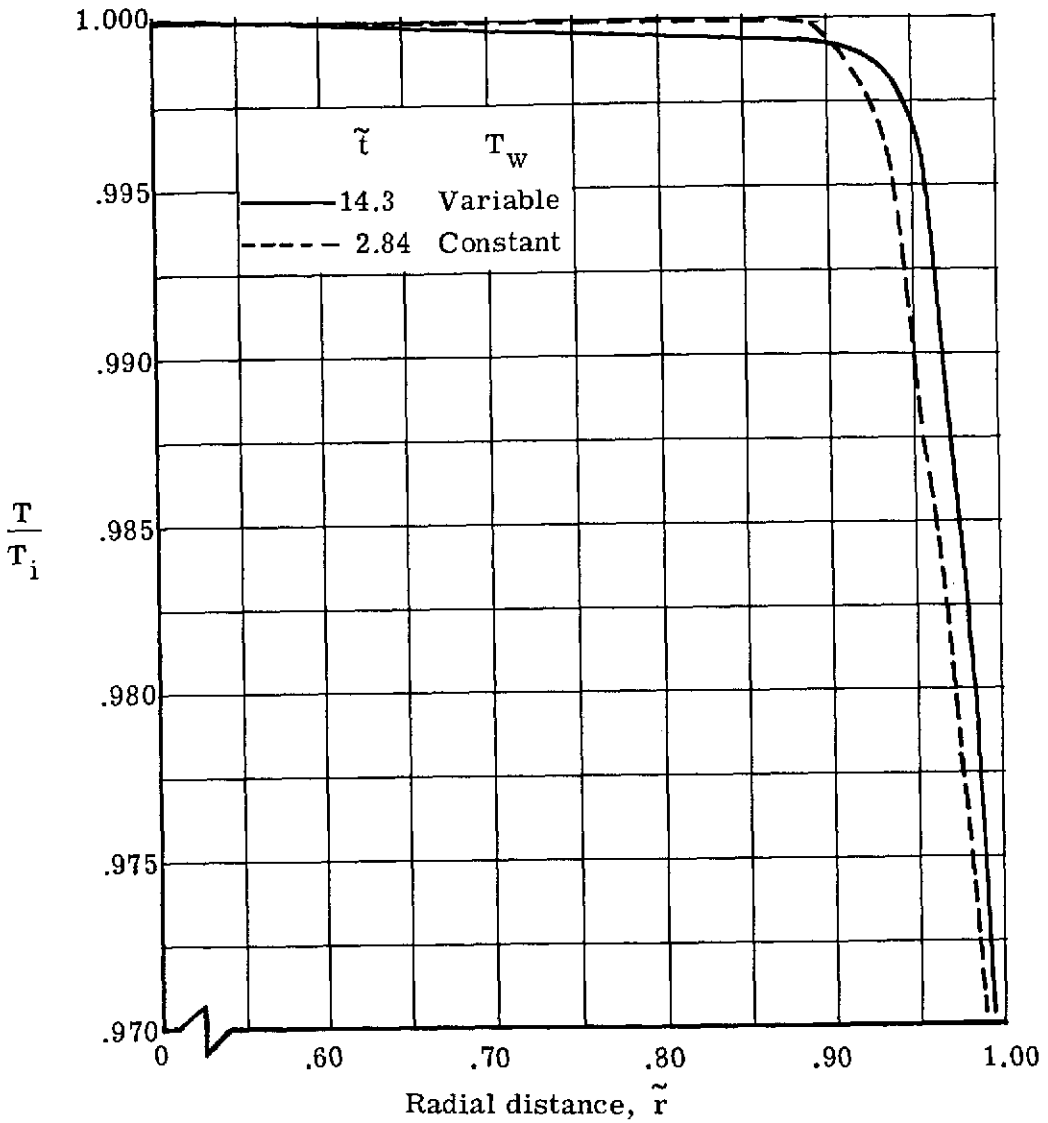

(b) Equal Grashof numbers $\left(N_{Gr} = 5 \times 10^7\right)$.

Figure 16.- Concluded.

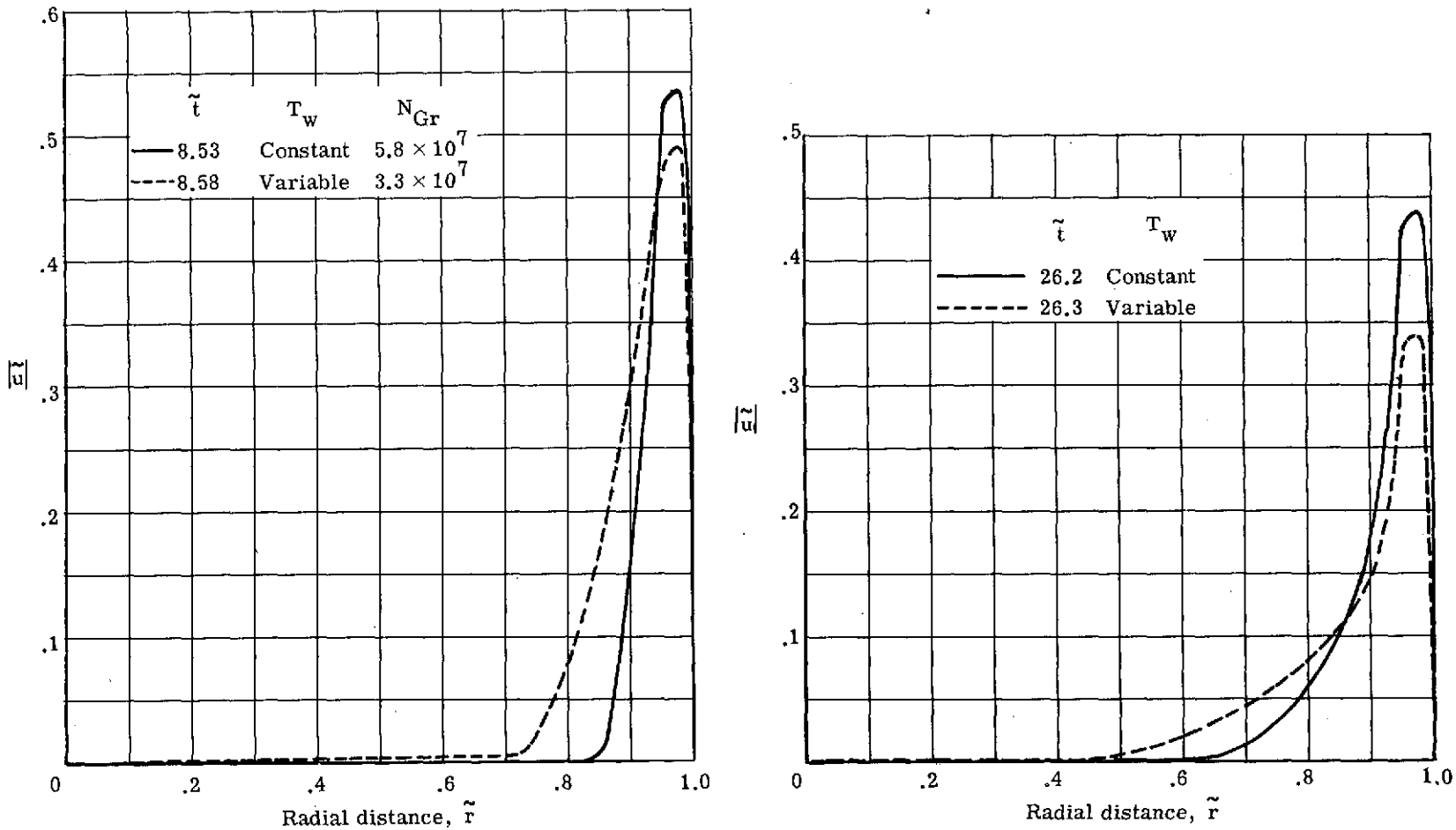

(a) Early time.

(b) Late time. $N_{Gr} = 5.8 \times 10^7$.

Figure 17.- Azimuthal velocity distributions for constant and variable wall temperature. Case I; $\theta = 90^o$.

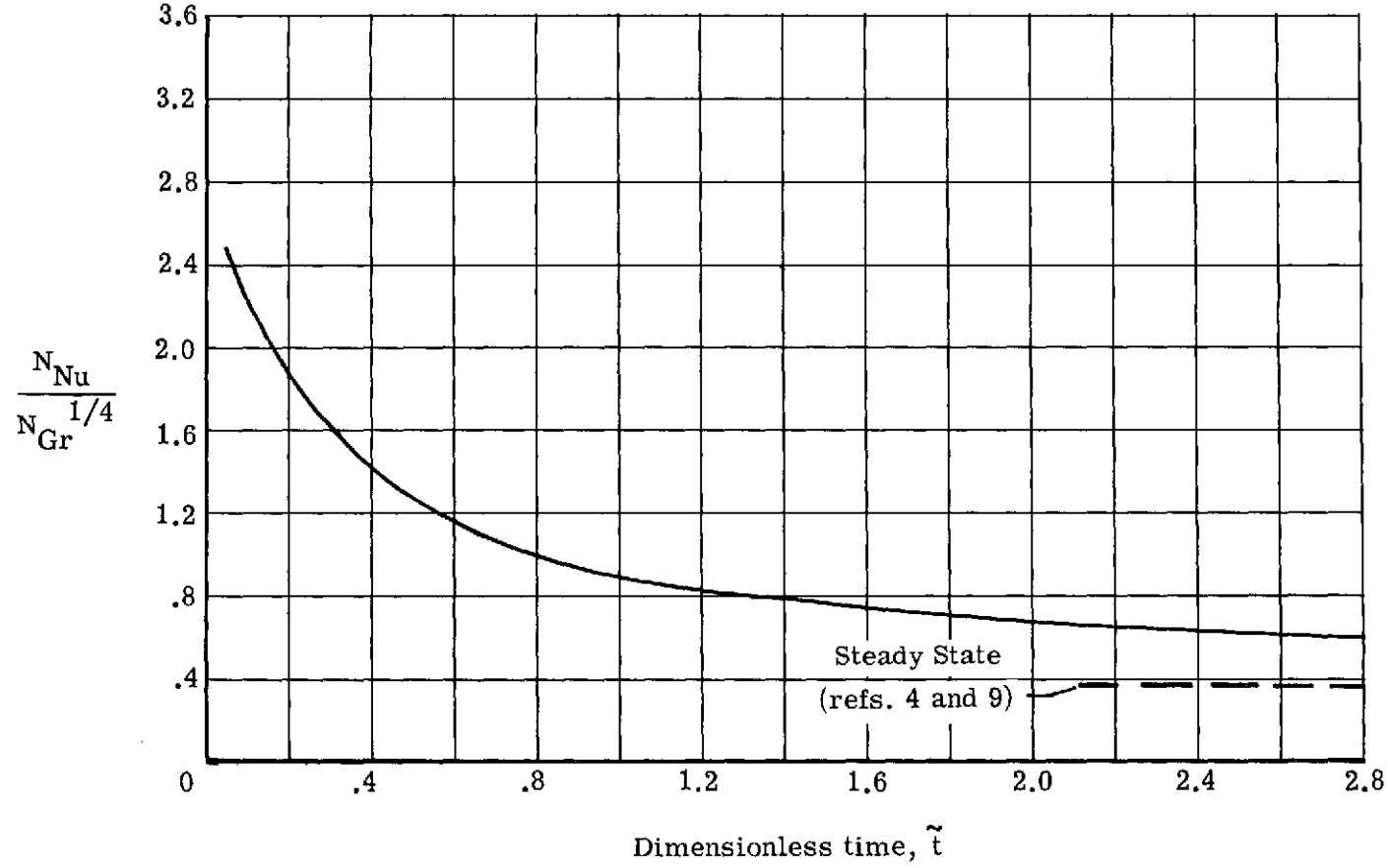

Figure 18.- Nusselt-Grashof correlation, averaged over the entire wall, for time-dependent flow within a horizontal cylinder. Case I; $(N_{Gr})_{max} = 5.8 \times 10^7$; $\left(\frac{T_w}{T_i}\right)_{min} = 0.936$.

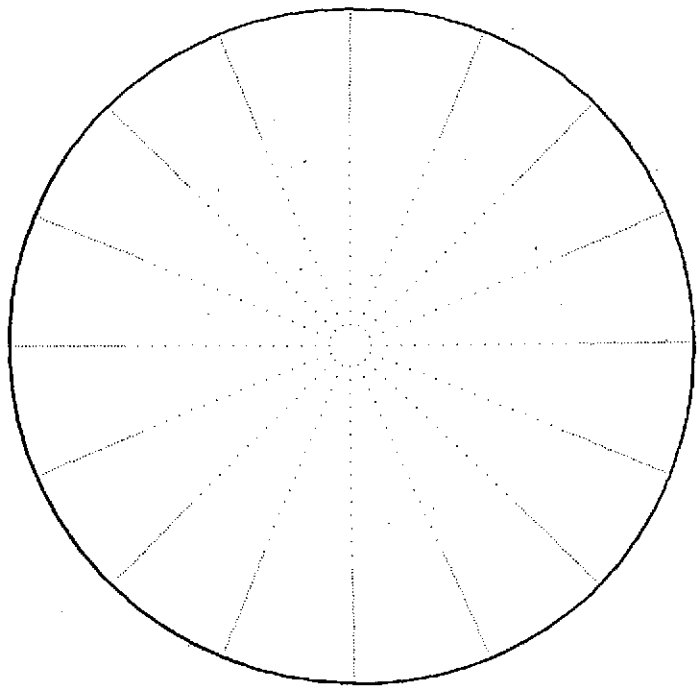

$t = 0$; $N_{Gr} = 0$

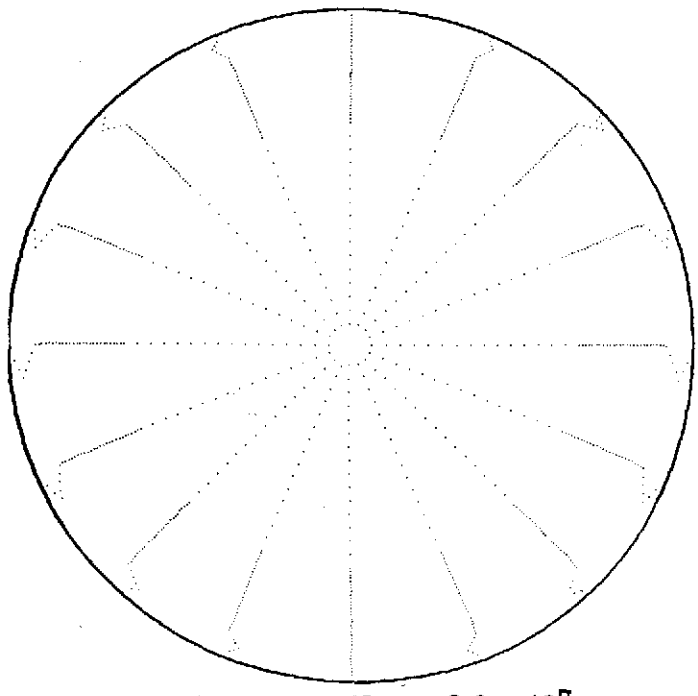

$t = 3.86$ sec; $N_{Gr} = 2.3 \times 10^7$.

(a) $t = 0$ and 3.86 sec.

Figure 19.- Oscilloscope photographs of fluid-element displacements from the numerical solutions for natural convection within a horizontal cylinder. Time-dependent wall temperature; case I.

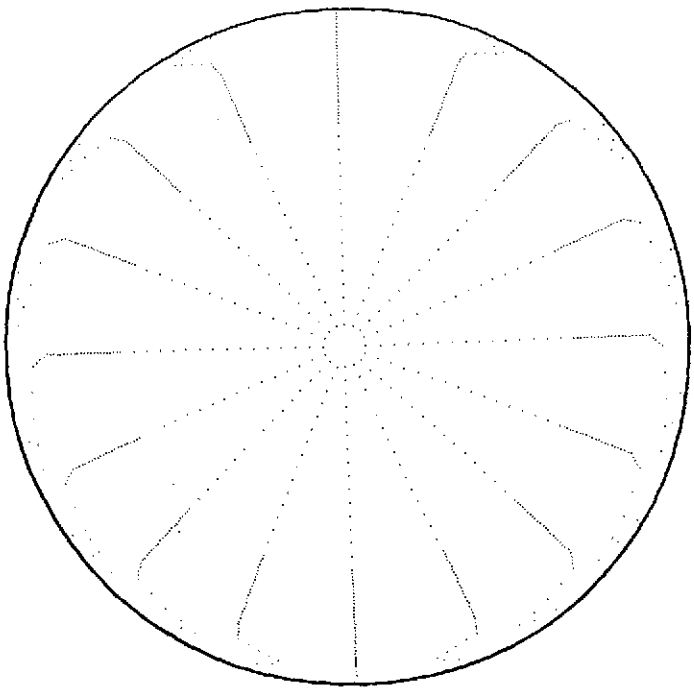

t = 5.13 sec; $N_{Gr} = 3.6 \times 10^7$

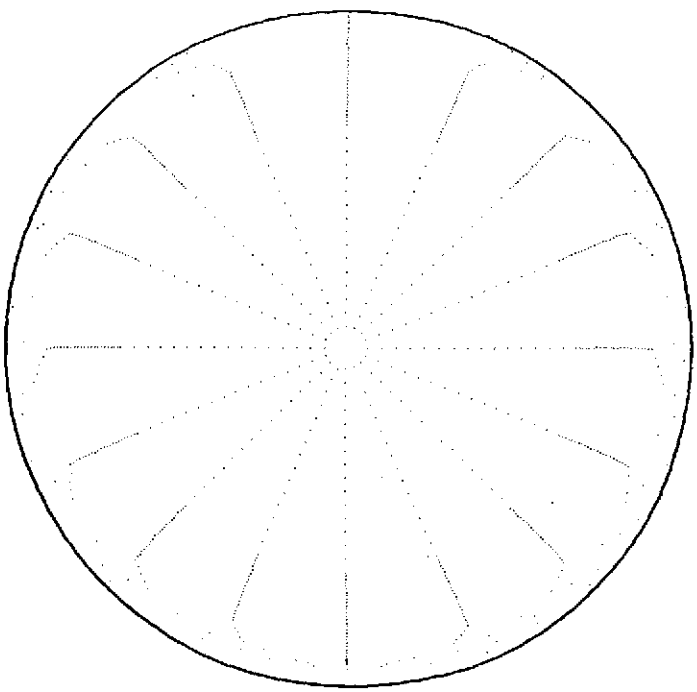

t = 6.15 sec; $N_{Gr} = 4.9 \times 10^7$

(b) t = 5.13 and 6.15 sec.

Figure 19.- Continued.

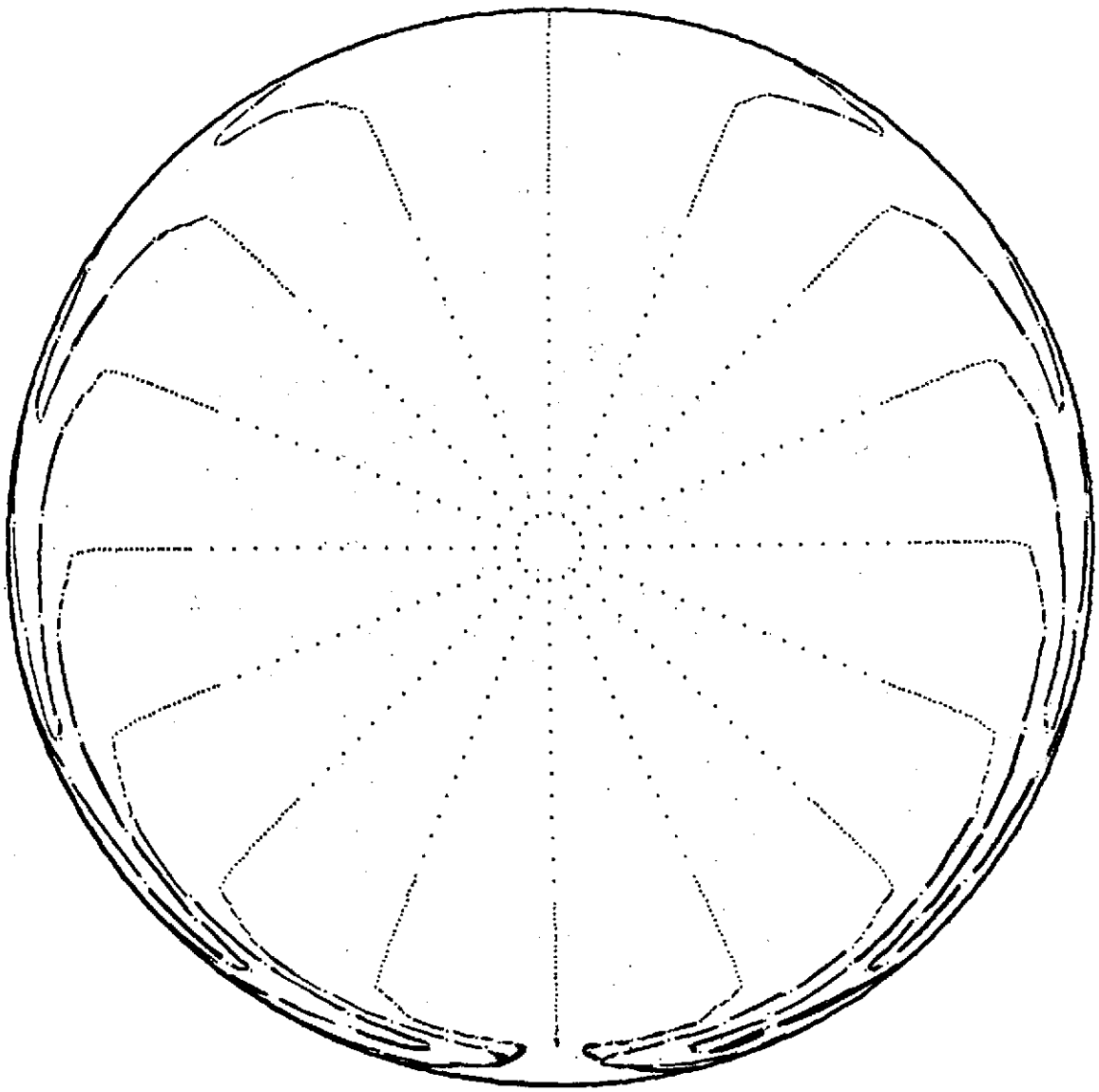

t = 6.6 sec; $N_{Gr} = 5.5 \times 10^7$

(c) t = 6.6 sec.

Figure 19.- Concluded.

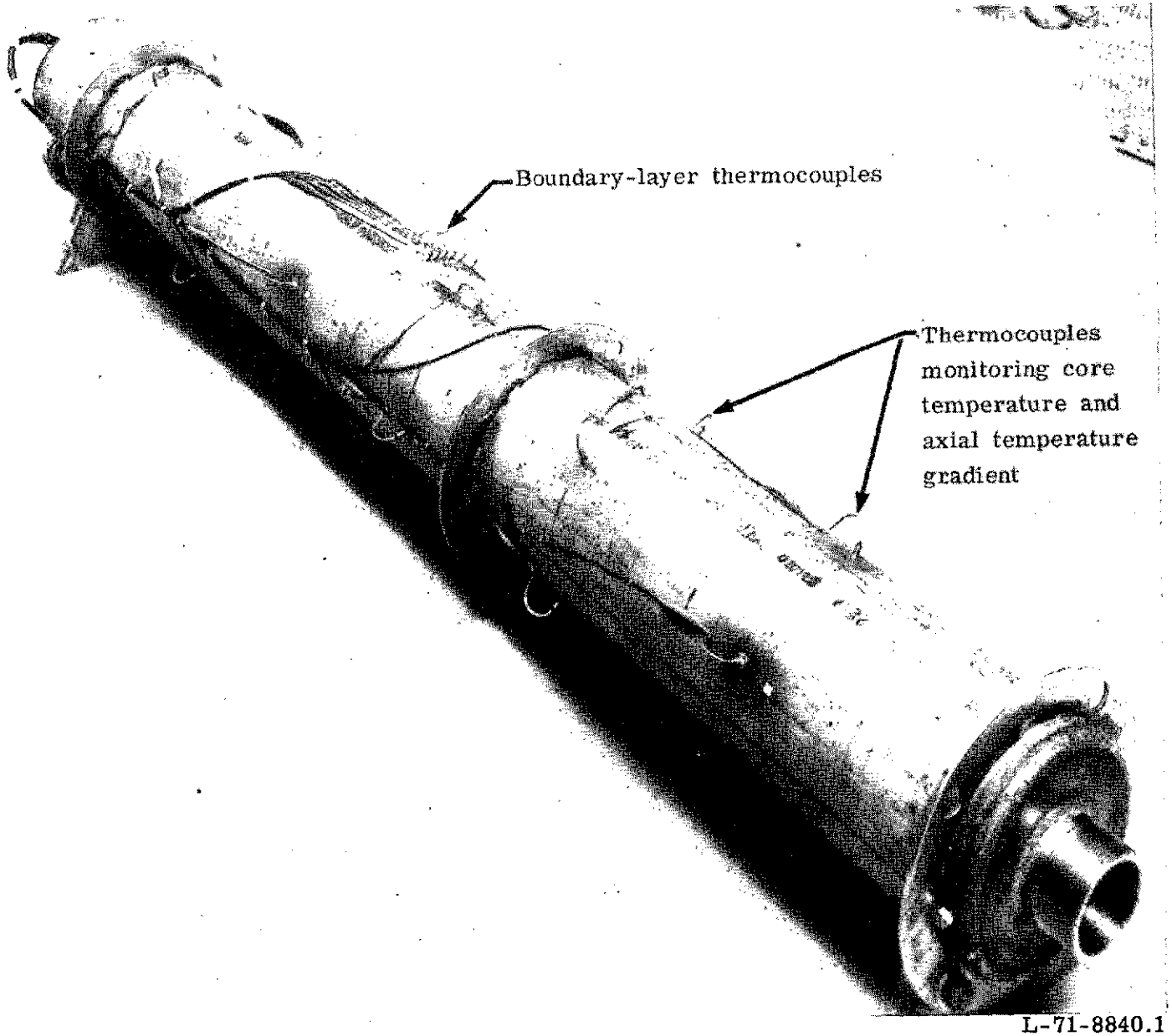

Figure 20.- Instrumented natural convection chamber.

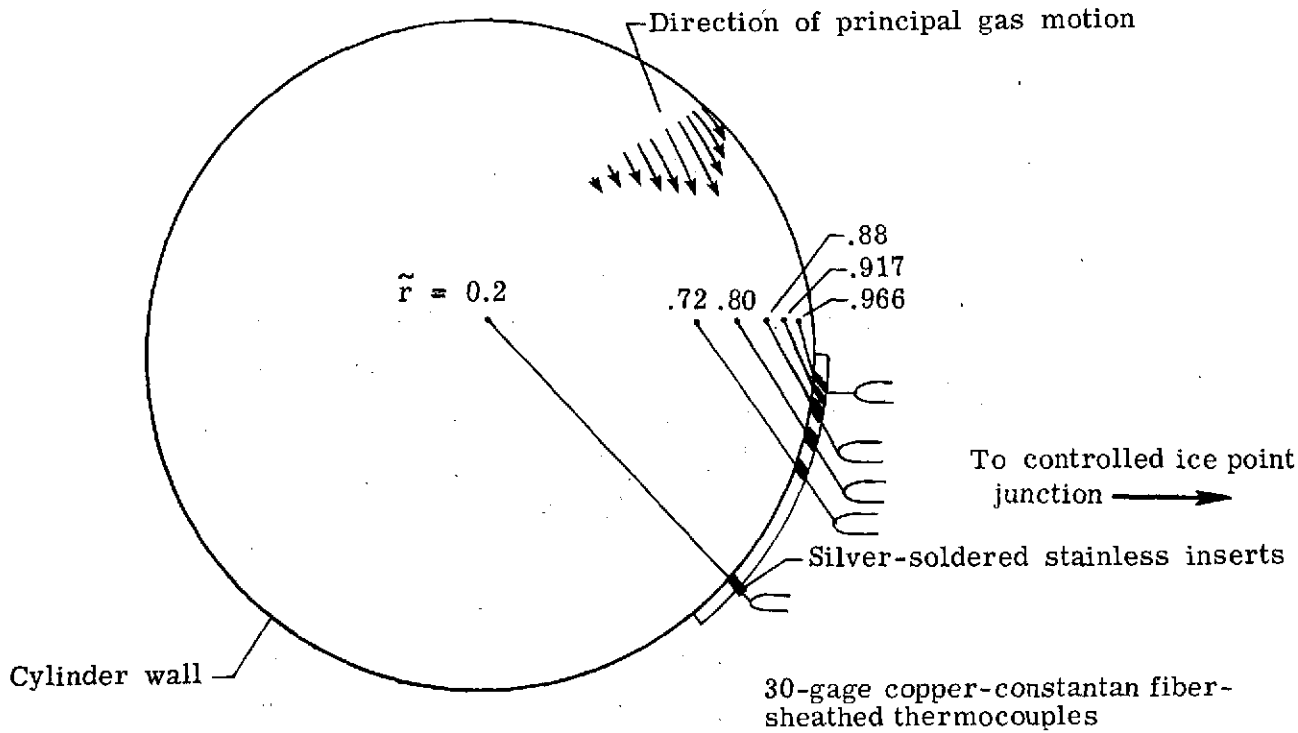

Figure 21.- Locations of boundary-layer and core thermocouples within horizontal cylinder.

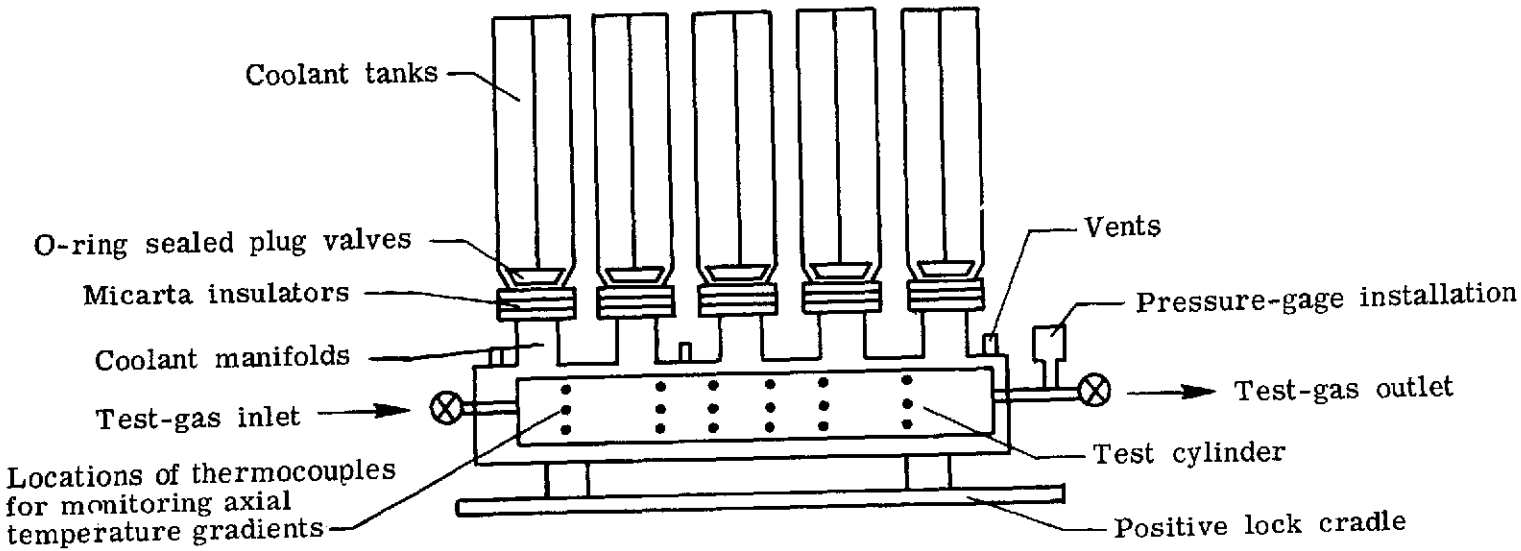

Figure 22.- Schematic diagram of apparatus for natural convection experiments.

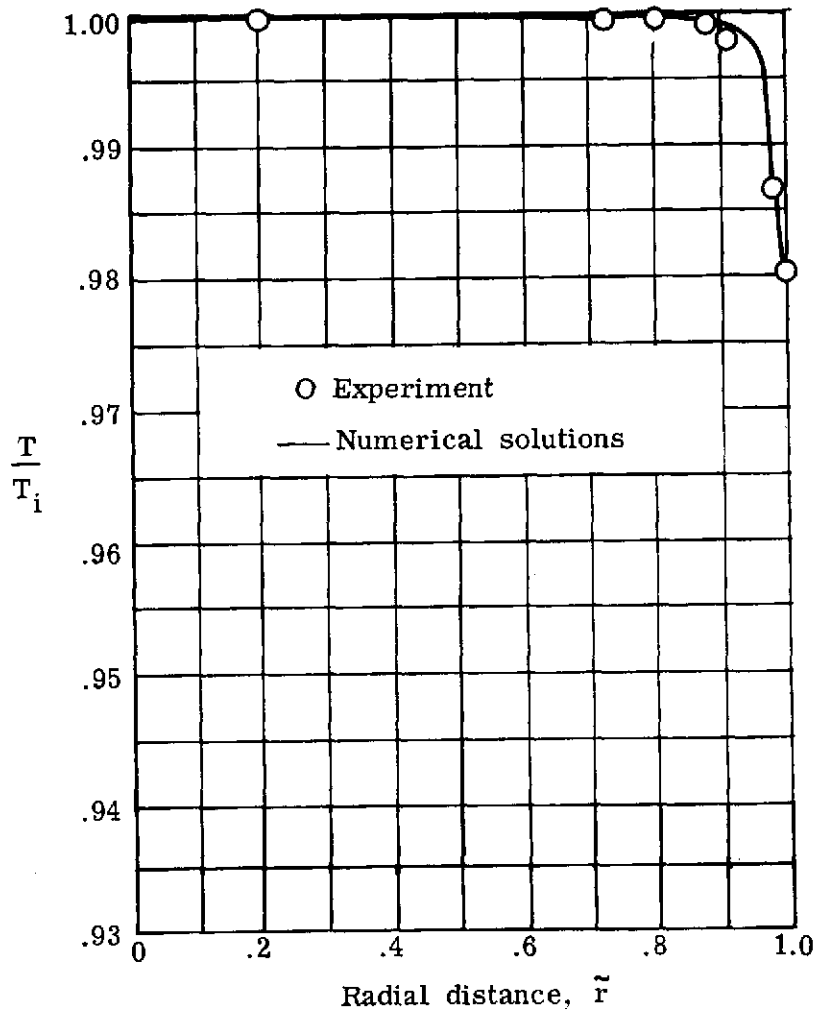

(a) t = 1.2 sec.

Figure 23.- Temperature distribution for a time-dependent wall temperature. Case I; $\theta = 90^{o}$.

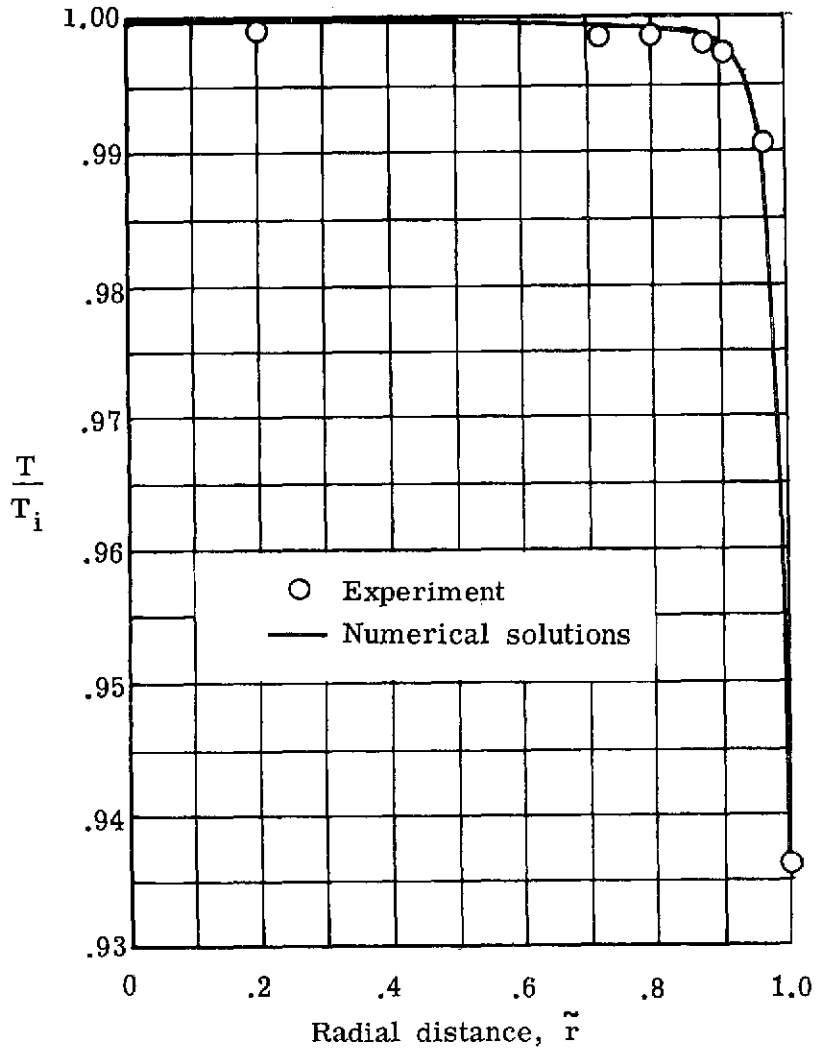

(b) t = 4.0 sec.

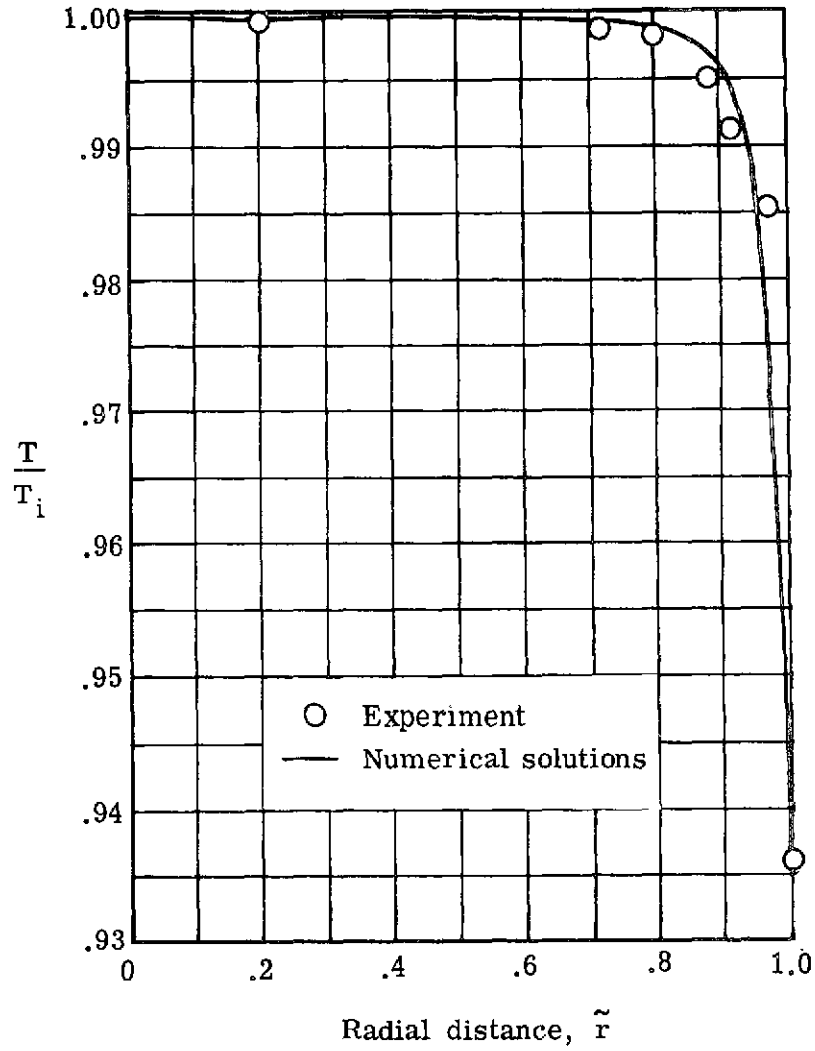

(c) t = 8.0 sec.

Figure 23.- Concluded.

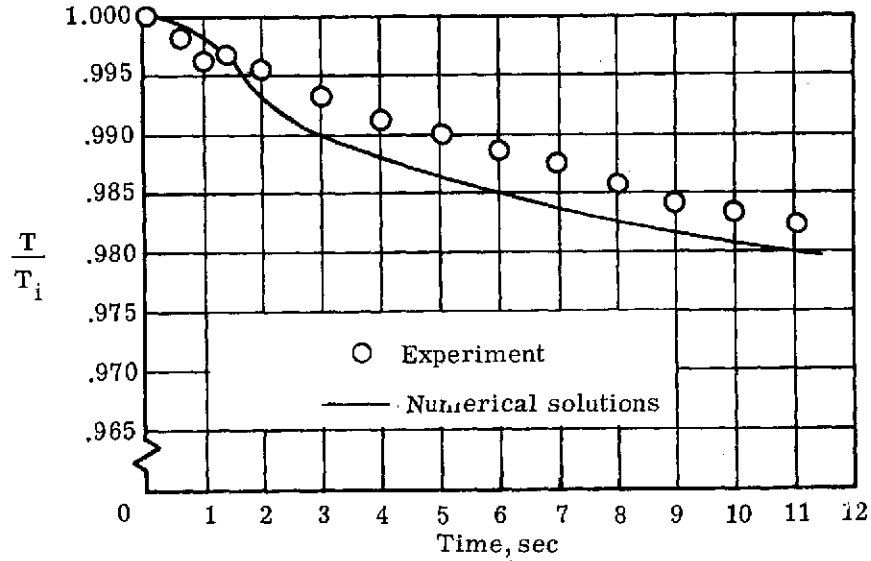

(a) $\theta = 90^{o}$.

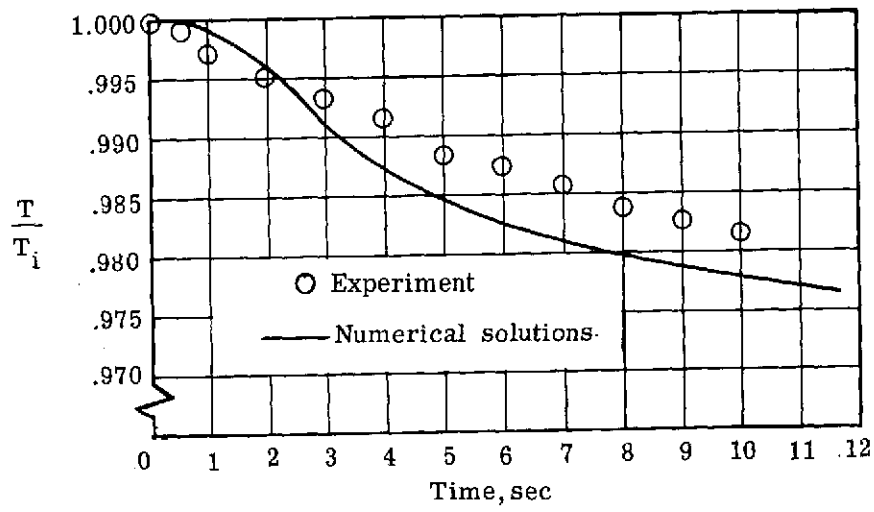

(b) $\theta = 70^{o}$.

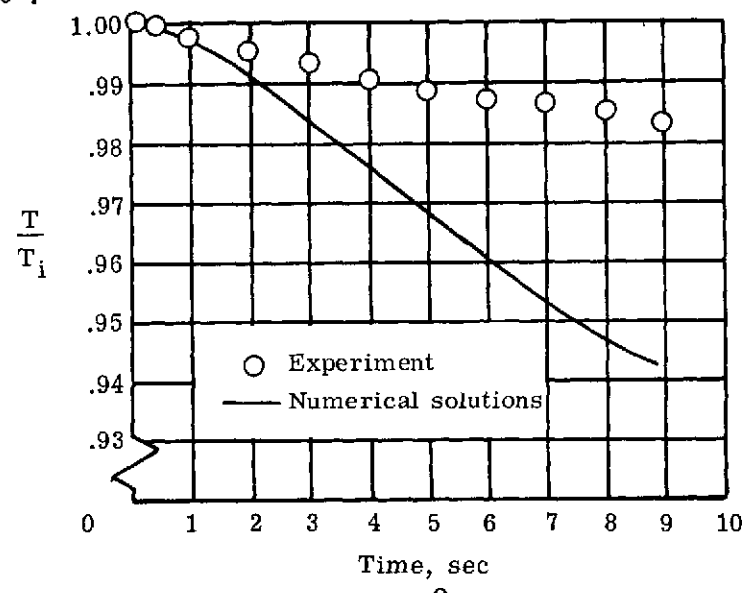

(c) $\theta = 0^{o}$.

Figure 24.- Boundary-layer temperature decay at $\tilde{r} = 0.966$. Case I; $(N_{Gr})_{max} = 6 \times 10^{7}$.

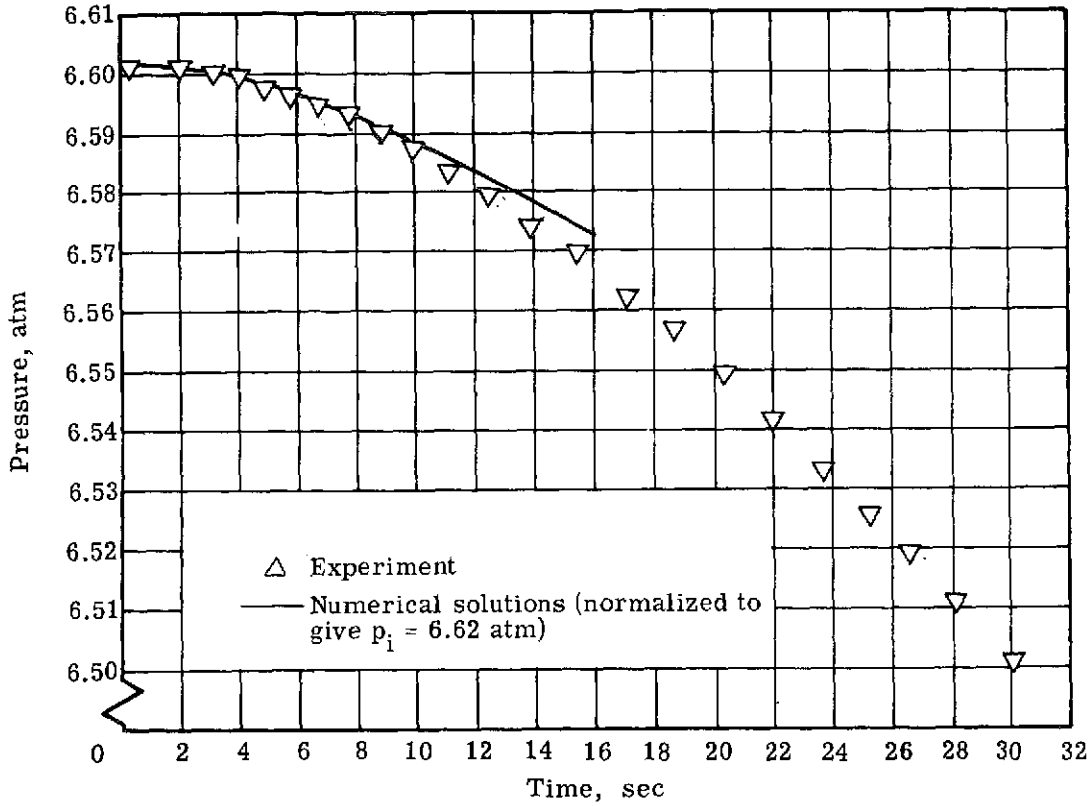

Figure 25.- Measured pressure decay due to natural convection within a horizontal cylinder. Case I; $\left(N_{Gr}\right)_{max} = 7 \times 10^7$.

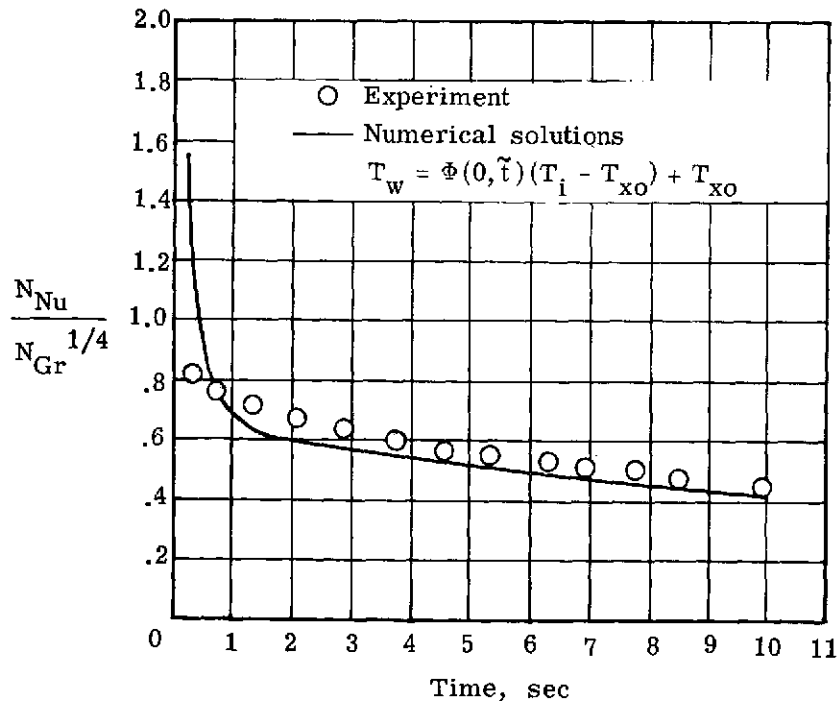

Figure 26.- Nusselt-Grashof relation for natural convection within a horizontal cylinder. Case I; $\left(N_{Gr}\right)_{max} = 7 \times 10^7$; $\theta = 90^o$.

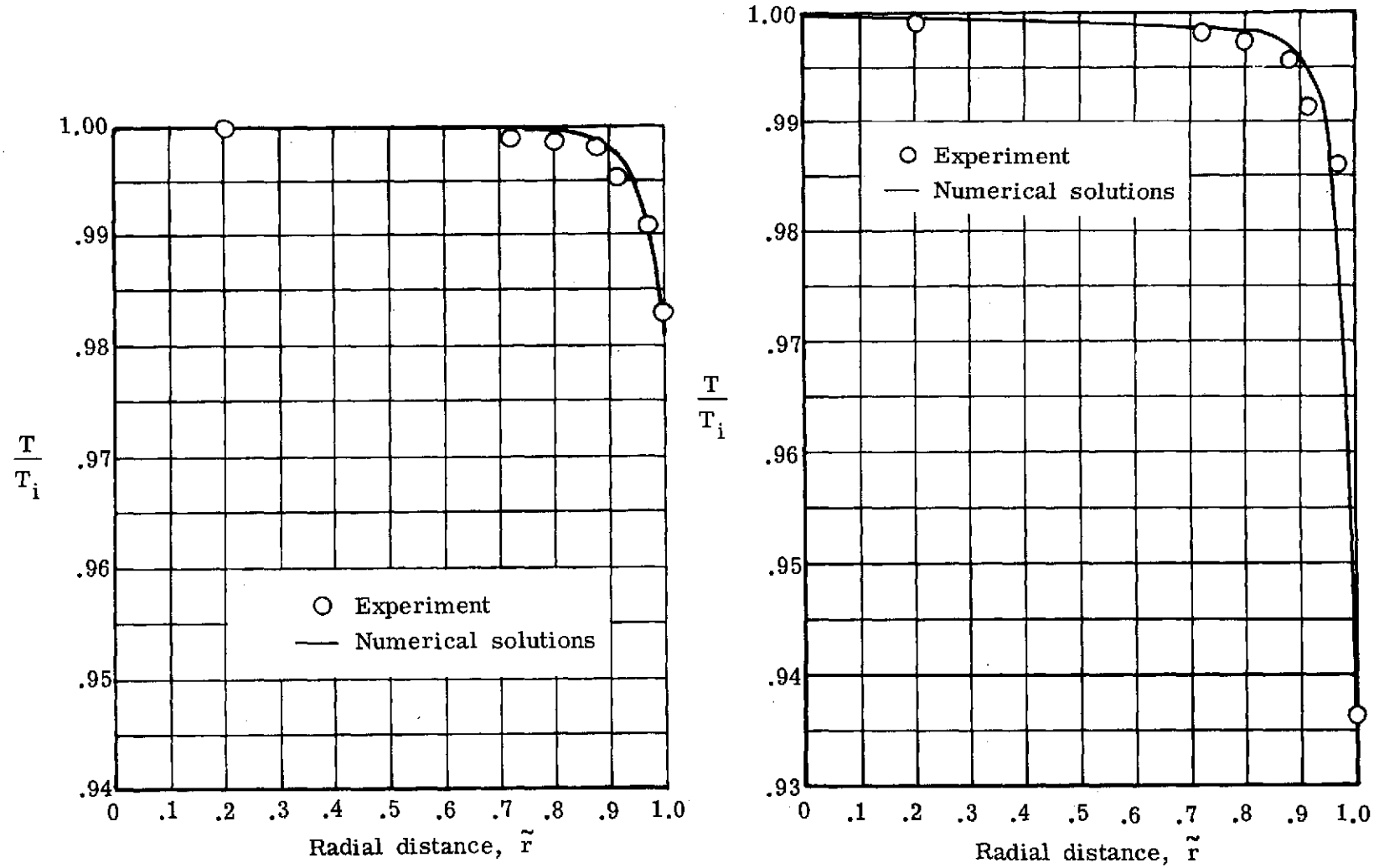

(a) t = 4.0 sec.

(b) t = 8.0 sec.

Figure 27.- Radial temperature distribution at $\theta = 90^{o}$. Case I; $(N_{Gr})_{max} = 6 \times 10^{7}$.

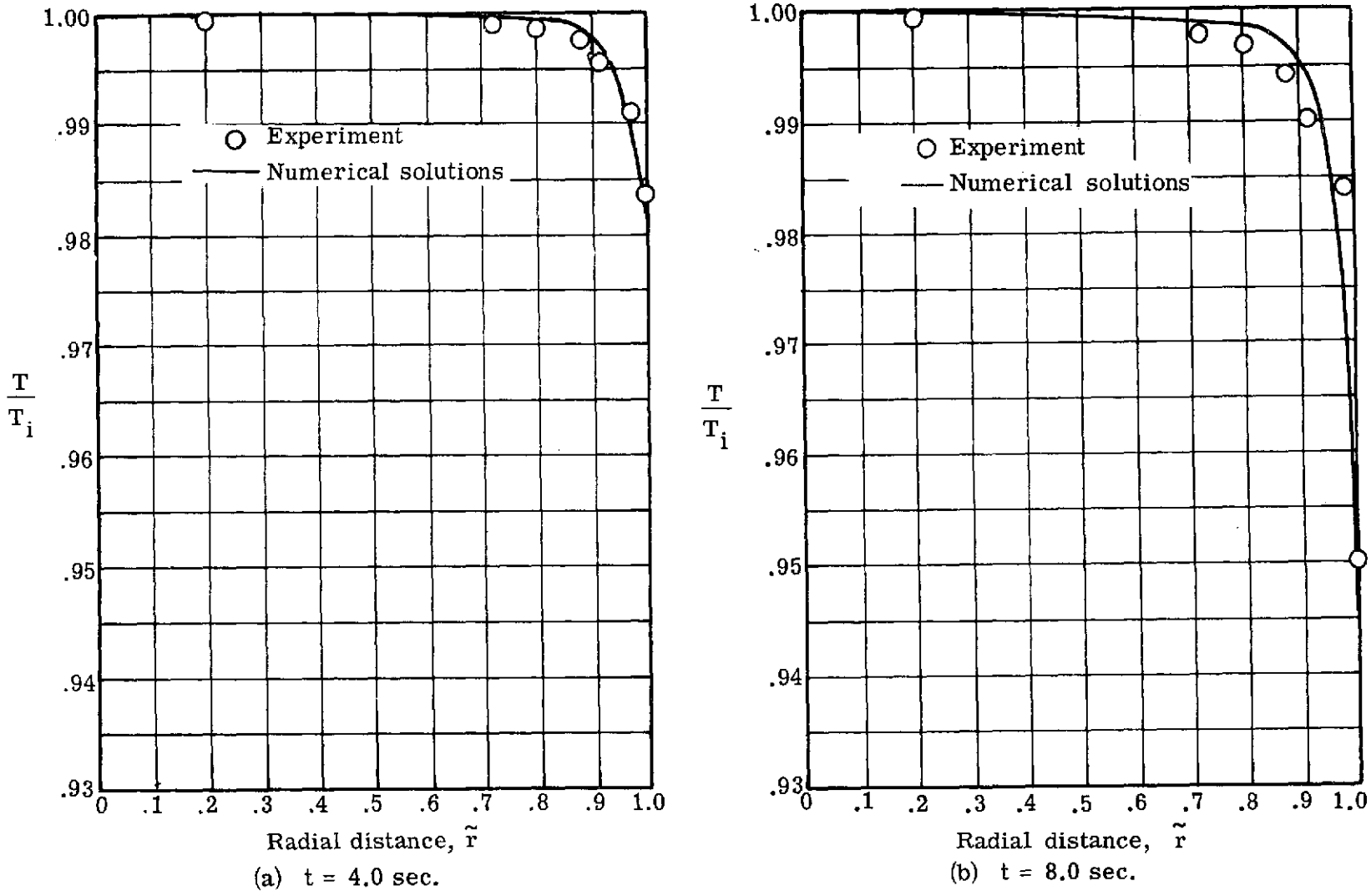

Figure 28.- Radial temperature distribution at $\theta = 70^{o}$. Case I; $(N_{Gr})_{max} = 6 \times 10^{7}$.

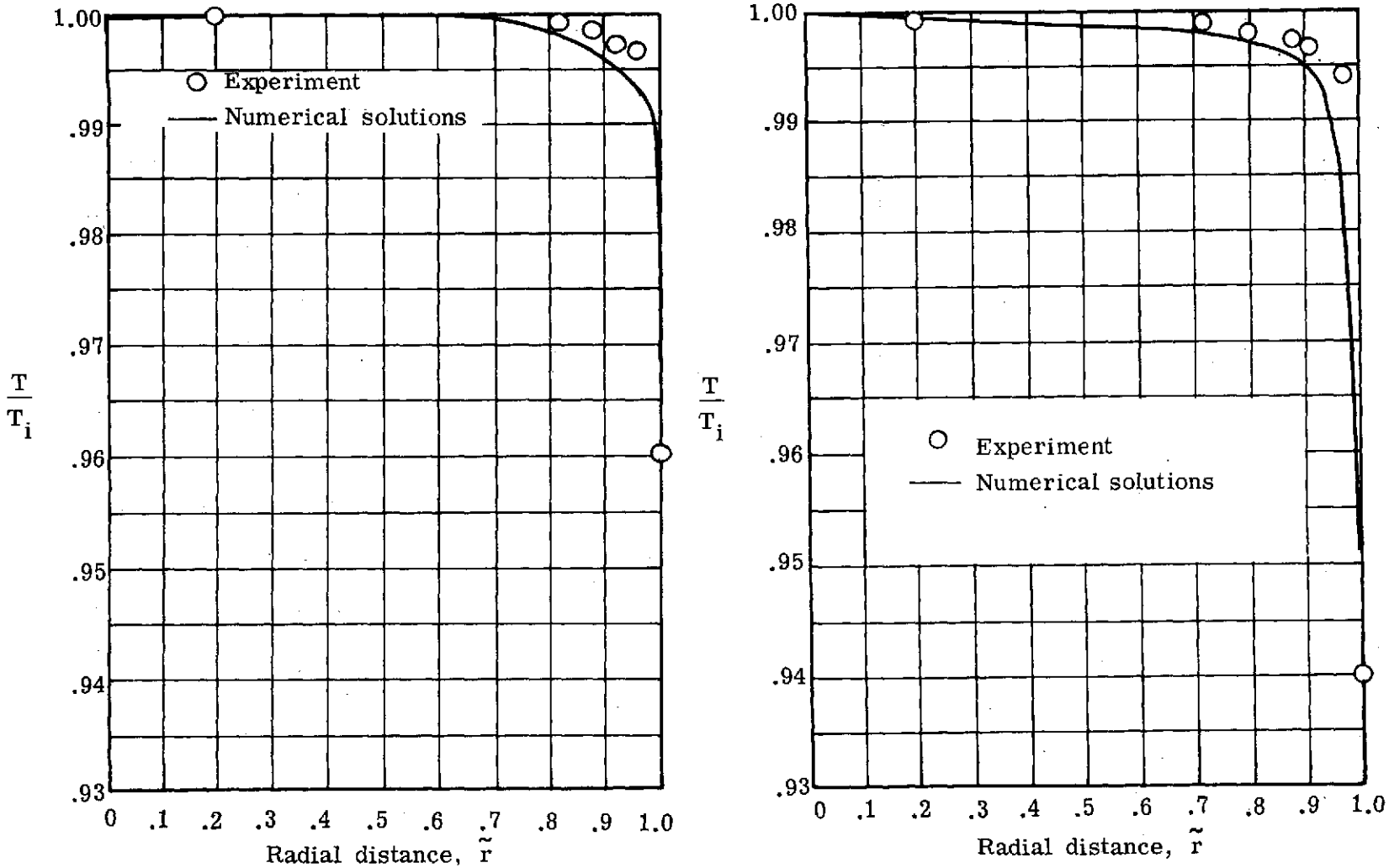

Figure 29.- Radial temperature distribution at $\theta = 90^{o}$. Case II.

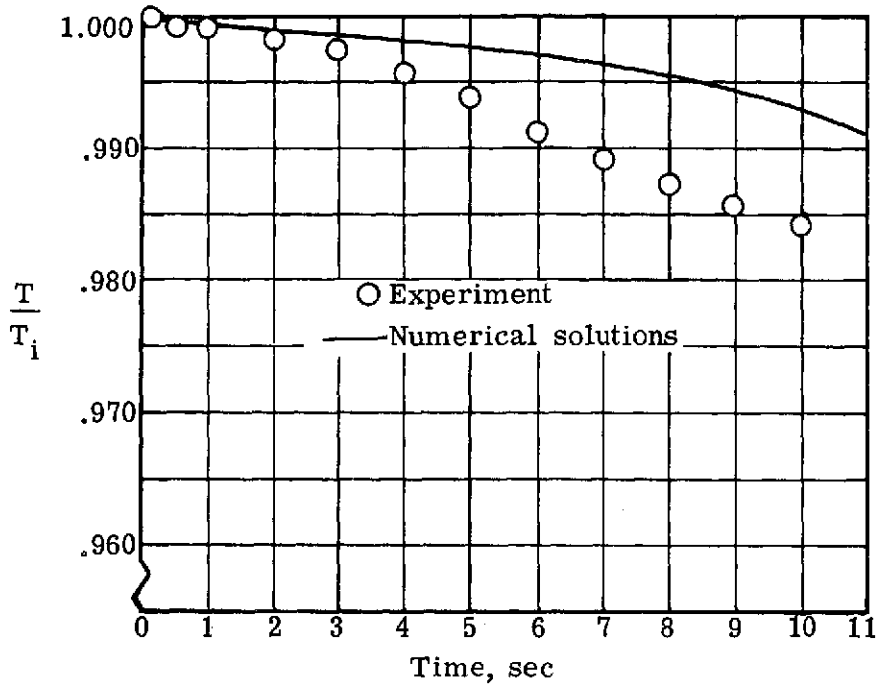

Figure 30.- Decay of boundary-layer temperature at $\theta = 90^{o}$, $\tilde{r} = 0.966$, and $(N_{Gr})_{max} = 1.3 \times 10^{6}$. Case II.

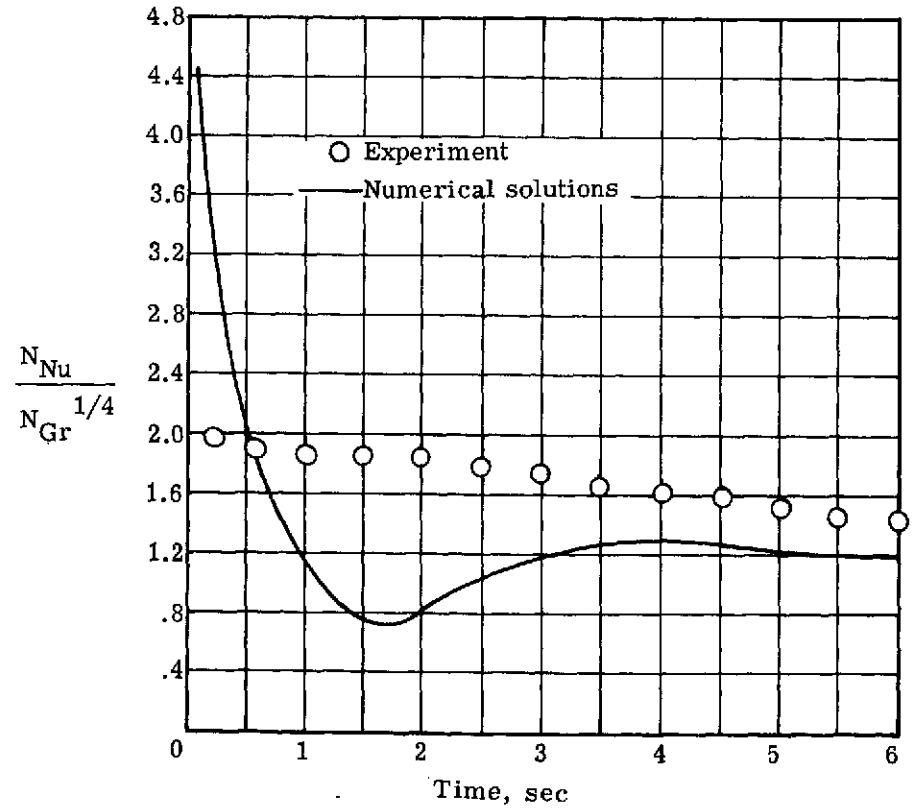

Figure 31.- Nusselt-Grashof relation for $\theta = 90^{o}$ and $(N_{Gr})_{max} = 6.5 \times 10^{5}$. Case II.

NASA-Langley, 1974 L-9652